

ABSTRACT

HALL, ANDREW MERRILL. Lifecycle Characteristics of Marine Stratocumulus Precipitation in the Southeast Pacific. (Under the direction of Sandra Yuter).

Cloud and precipitation processes in the marine stratocumulus environment of the Southeast Pacific play a key role in the Earth's energy budget. Low clouds in these regions are typically widespread, long lived, and reflect a large fraction of incoming solar insolation. Precipitation offers a potential avenue for liquid water to be removed from the cloud layer and is thought to be associated with cloud breakup, especially. Understanding how precipitation and marine cloud cover interact is necessary to fully understand the global impacts of this region. The goal of this work is to analyze the behaviors of precipitation cells and connections between precipitation and cloud breakup. In order to fully understand how precipitation develops, a significant portion of this study is the development of a precipitation cell tracking algorithm that will work in a region with very high spatial and temporal variability of precipitation.

Radar precipitation data were collected during the Variability of the American Monsoon Systems (VAMOS) Ocean Cloud-Atmosphere-Land Study Regional Experiment (VOCALS-REX). Data was collected continuously, over a period of 21 days, by a scanning C-band radar and several other instruments on board the National Oceanic and Atmospheric Administration's ship the Ronald H. Brown. These data were used to examine strong precipitation cores (> 5 dBZ) in the vicinity of 20°S , off the coast of Chile. The joint variability of satellite-determined local cloudiness and radar-determined precipitation patterns are used to determine connections between the two systems.

Consistent with previous work, precipitation overnight, in broken, non-overcast cloud conditions is shown to contain higher frequencies of strong precipitation events than precipitation during daytime or overcast conditions. However, the median behavior of precipitation cores does not vary significantly across the diurnal cycle and is not strongly related to local cloud condition. Cloud breakup overnight is shown to occur with or without large areas of strong precipitation present. This suggests that precipitation is not a necessary condition for overnight cloud breakup. The distributions of size and intensity of marine stratocumulus precipitation in the Southeast Pacific are similar to other buoyancy-driven regions, including trade cumulus and weak tropical convection.

© Copyright 2013 Andrew Merrill Hall

All Rights Reserved

Lifecycle Characteristics of Marine Stratocumulus Precipitation in the Southeast Pacific

by

Andrew Merrill Hall

A thesis submitted to the Graduate Faculty of
North Carolina State University
in partial fulfillment of the
requirements for the degree of
Master of Science

Marine, Earth, and Atmospheric Science

Raleigh, North Carolina

2014

APPROVED BY:

Sandra Yuter
Committee Chair

Walt Robinson

Matthew Parker

Table of Contents

List of Figures	v
Chapter 1 Introduction	1
Chapter 2 Data	6
2.1 Radar Data	6
2.2 Additional Data.....	7
Chapter 3 Methods	10
3.1 Precipitation Core Identification.....	10
3.2 Feature Detection.....	11
3.3 Tracking Method.....	13
Chapter 4 Results	21
4.1 Data Set Statistics	21
4.2 Bulk Track Statistics	26
4.3 Diurnal Cycle and Cloud Fraction.....	38
4.4 Cell Lifecycle.....	41
4.4.1 Signs of Internal Organization	43
4.5 Mesoscale Structure and Cell Proximity.....	50
4.6 Comparisons to Other Types of Convection.....	56
4.7 Precipitation and Cloud Breakup.....	61
Chapter 5 Conclusions	69
References	72

List of Figures

Chapter 2

Figure 2.1 NOAA Research Vessel Ronald H. Brown's movement.....1

Chapter 3

Figure 3.1 Step-by-step filtering process19

Figure 3.2 Simplified example of the four main steps involved in the feature tracking algorithm.....20

Chapter 4

Figure 4.1 Histogram of radar sampling hours for each cloud state24

Figure 4.2 Average number of precipitation cores for each cloud state across the diurnal cycle.....25

Figure 4.3 Track overview for sample track occurring on 27 Oct 2008 at 17:12 UTC30

Figure 4.4 Track overview for sample track occurring on 28 Oct 2008 at 23:06 UTC31

Figure 4.5 Track overview for sample track occurring on 27 Oct 2008 at 14:33 UTC32

Figure 4.6 Track velocity and track travel directions for tracks longer than 30 minutes.....33

Figure 4.7 Frequency and cumulative distributions of tracked cell properties for tracks longer than 15 minutes.....34

Figure 4.8 Cell characteristic terms and definitions.....35

Figure 4.9	Distribution of peak cell intensity versus median area and versus duration	36
Figure 4.10	Venn diagram of tracked cell behaviors	37
Figure 4.11	Distribution of peak intensities separated by cloud condition and diurnal cycle	40
Figure 4.12	Frequency distribution of track intensity changes over observed lifetime for tracks greater than 30 minutes	45
Figure 4.13	Frequency distribution of track intensity changes for real tracks versus simulated tracks of length 42 minutes	46
Figure 4.14	Frequency distribution of track area changes over observed lifetime for tracks greater than 30 minutes	47
Figure 4.15	Frequency distribution of track intensity changes for night and day tracks	48
Figure 4.16	Frequency distribution of front-to-rear differential max intensity for tracks greater than 30 minutes	49
Figure 4.17	Cell location examples for three random and two observed cell distributions.....	52
Figure 4.18	Histogram of number of precipitation cores per radar frame for frames with at least 2 cores.....	53
Figure 4.19	Distribution of unique minimum distance between observed cells and two idealized distributions	54

Figure 4.20	Probability density curves for unique minimum distance for day, night, overcast, and non-overcast.....	55
Figure 4.21	Log-log distributions of number of cells for VOCALS and RICO.....	58
Figure 4.22	Distribution of mean cell intensity versus area for VOCALS and RICO	59
Figure 4.23	Histogram of fractional precipitation area for VOCALS and Lopez (1975).....	60
Figure 4.24	Observed number of cloud transitions versus average precipitation area.....	66
Figure 4.25	Cumulative probability of cloud transition occurring with less than or equal to a given precipitation area	67
Figure 4.26	Cumulative probability of cloud transition occurring with less than or equal to a given precipitation area separated for day and night	68

Chapter 1

Introduction

Marine stratocumulus clouds occur in the subtropical ocean regions off the west coast of continents. Clouds in these regions form at the top of the marine boundary layer, between a cool, moist surface layer and a strong stable layer sitting 1.5 – 2 km above the ocean surface. The large-scale, downward motions of the Hadley cell create a strong, shallow temperature inversion which limits vertical cloud development in the region (Emanuel et al 1994). The stratocumulus cloud decks cover areas that are tens of degrees in latitude and longitude and represent a significant portion of the overall earth system cloudiness at any time (Klein and Hartmann 1993). The relatively large, unbroken expanse of clouds reflects a considerable amount of solar energy. The relatively short vertical extent of the clouds means that the cloud top temperatures are not significantly different from surface temperatures (~5-8 degrees Celsius) and therefore emit long wave energy at roughly the same intensity as the surface (Hartmann et al. 1992). This combination means these clouds have a net cooling effect and are therefore important to the global energy balance across a broad range of timescales, from daily to annually. The marine stratocumulus regions remain a major uncertainty in global climate models due to difficulties in properly modeling the spatial and temporal development of cloudiness (Bony et al. 2006, Wyant et al 2006). Marine stratocumulus clouds are pervasive and persistent in the particularly in the Northeast and Southeast Pacific and the

Southeast Atlantic. The Southeast Pacific is of particular interest because it shows, amongst the three main regions, the highest area and temporal cloud fractions (Klein and Hartmann 1993, Frey 2013).

The predominant factor in regional reflectivity is simply the spatial and temporal coverage of cloud (Stephens and Greenwald 1991, de Szoeke et al. 2012). On the cloud scale, the differences between individual clouds in the stratocumulus region are minimal. Clouds in this region can have relatively high variations (>50%) in cloud droplet concentration, aerosol content, and liquid water path without changing the cloud albedo significantly (George and Wood 2010). Despite the calm, quiescent appearance of the slowly changing stratocumulus cloud fields, the meteorology is the complex sum of many parts. Factors involved in synoptic scale cloud development involve elements from large scales like subsidence strength (Zhang et al. 2009) to small scale aerosol effects (Albrecht 1989, Pincus and Baker 1994). Cloud transitions have also been linked to temporal elements such as the diurnal cycle (Burleyson et al 2013) and seasonal changes in stability (Klein and Hartmann 1993). More transient contributions like density currents (Feingold et al. 2010, Terai and Wood 2013, Wilbanks 2013), gravity waves (Allen et al. 2012), and other wavelike propagations (aka “the upsidence wave”, Garreaud and Munoz 2004) have been proposed to have an effect on marine stratocumulus precipitation and cloud structure.

Where clouds are present in the region they fall into two types; closed cells and open cells (Atkinson and Zhang 1996). Closed cells are regions of continuous stratus and stratocumulus

clouds without any significant breaks between clouds. Open cells are regions of isolated stratocumulus clouds with clearing between them. The clearing means that the high albedo cloud deck is no longer present which in turn, offers a direct pathway for solar radiation to be absorbed into the ocean system. The creation of a pocket of open cells (POCs def. as “open cell region surrounded by closed cells”, Bretherton et al. 2004, Stevens et al. 2004) is hypothesized to be linked with strong nocturnal precipitation. This cloud breakup overnight can lead to overall lower cloud cover as dawn breaks. Decreased regional cloudiness means decreased overall regional reflectance and a corresponding increase in solar insolation that reaches the surface (Burleyson 2013). A mechanism for the overnight cloud breakup is currently hypothesized to be related to depletion (sedimentation) of aerosol (Berner et al. 2013) and moisture depletion through a combination of sub-cloud stabilization (Bretherton and Wyant 1997) and precipitation reaching the surface (Stevens et al. 2005b, Wang and Feingold 2009). The Variability of the American Monsoon System (VAMOS) Ocean Cloud Atmosphere Land Study and Regional Experiment (VOCALS-REX, Wood et al 2011b) which took place in the Southeast Pacific during October and November of 2008, was both an attempt to answer questions about the importance of POCs and the primary source of data for this study.

Understanding how precipitation develops and what factors modulate it are key components of understanding the evolution of the marine stratocumulus regions. To this end, we wanted to better understand the individual lifecycles of precipitation cells and hence, needed an automated method of tracking them. The concept of feature tracking developed in the 1980s

out of a desire to track individual radar and satellite features. Two general design philosophies exist when looking at existing feature tracking methods (Lakshmanan and Smith 2010); cost minimization or score maximization, though the differences are mostly conceptual. The earliest automated tracking methods used in radar meteorology applications (Dixon and Wiener 1993, Johnson et al. 1998) reduced the tracked feature to a single centroid located at the “center of effect” of the feature. These methods are used with good effect for hindcasting and nowcasting severe storm movement and usually involve thresholding the radar data at relatively high values (~25-35 dBZ). These methods seek to minimize a cost function to best associate a past cell with a future cell. Other feature tracking methods (Morel and Senesi 2006) use a score maximization approach in an attempt to maximize area or volume similarity, but without regard to intensity values. These methods include some consideration for the size similarity of features between sample times, but still favor features that do not change significantly in area or shape, like the convective cores of strong convection. For this work, we build on previous feature tracking methods to develop a tracking algorithm that can handle a broad range of reflectivity values (5 – 45 dBZ) and the close proximity of precipitation cores in marine stratocumulus.

This study uses ship-based radar and satellite IR data, obtained during VOCALS in the Southeast Pacific, to address the following questions:

- 1) What is the relative importance of several previously hypothesized modulating factors for precipitation in marine stratocumulus?

- 2) What organizational paradigms exist with regards to precipitation and cloudiness?
- 3) What similarities exist between marine stratocumulus precipitation and other types of convective precipitation?

Chapter 2

Data

This study uses data collected during the VOCALS-REX research cruise from October to December 2008 (Wood et al. 2011b, Mechoso et al. 2013). The primary data sets were collected by instruments on the NOAA research vessel Ronald H Brown (RHB). The ship collected data continuously during two separate cruise legs, the first from 25 October 2008 until 2 November 2008 and the second from 10 November 2008 until 2 December 2008 (Figure 2.1). The total data collection time was approximately 31 days. The ship-born instruments collected in-situ data of multiple atmospheric variables as well as remotely sensed data using active radar and lidar (Wood et al 2011b).

2.1 Radar Data

The predominant source of data for this study is the C-band precipitation radar that was aboard the RHB (Ryan et al. 2002). The radar data set represents a detailed record of the precipitation within 60 km of the ship during the VOCALS cruise. This instrument collected plan position indicator (PPI), full volume scans to a range of 60 km and a set of four range height indicators (RHI) every three minutes. The C-band radar is a 5.36 cm wavelength radar with a 0.95° beam width (Ryan et al. 2002) that is sensitive to light precipitation and

drizzle but does not detect cloud droplets. The original polar coordinate data were quality controlled to remove most non-meteorological echo and interpolated to Cartesian space at 250 m horizontal and 500 m vertical grid spacing. The stratocumulus clouds in this study range from a few km² to tens of km² in horizontal scale, so at this resolution precipitation cells will typically occupy 16 or more horizontal pixels. Further details on the radar data processing are provided in Appendix A of Burleyson et al. 2013. Because of the continual data collection, this data set is unique in the ability to observe marine stratocumulus precipitation throughout the diurnal cycle and across a relatively large region.

2.2 Additional Data

GOES Infrared satellite data were used to reference the observed radar domain against the sky condition above the same domain. Based off of METAR cloud observational doctrine (World Meteorological Organization 2008), four general classifications were applied and are used throughout this work. The four categories were determined by examining the satellite field in the same region as the radar domain. The four classifications are overcast (OVC) meaning 100% cloudiness, broken (BKN) ranging from 75% to 99%, scattered or less (SCT<) which is anything short of 75% and transition periods (TRN) determined by strong temporal variability in the values or when the ship itself moved into or out of an area of broken cloud. Cloud classification was determined every 4 hours and checked against an automated low cloud fraction algorithm described in Burleyson (2013).

Wind direction and speed is relatively constant throughout the VOCALS research period (d Szoeké et al. 2012). The wind velocity at the cloud level is $7 - 8 \text{ ms}^{-1}$ with a standard deviation of 3 ms^{-1} . The wind direction is also nearly constant throughout the study with a mean direction from 125 degrees (east southeasterly).

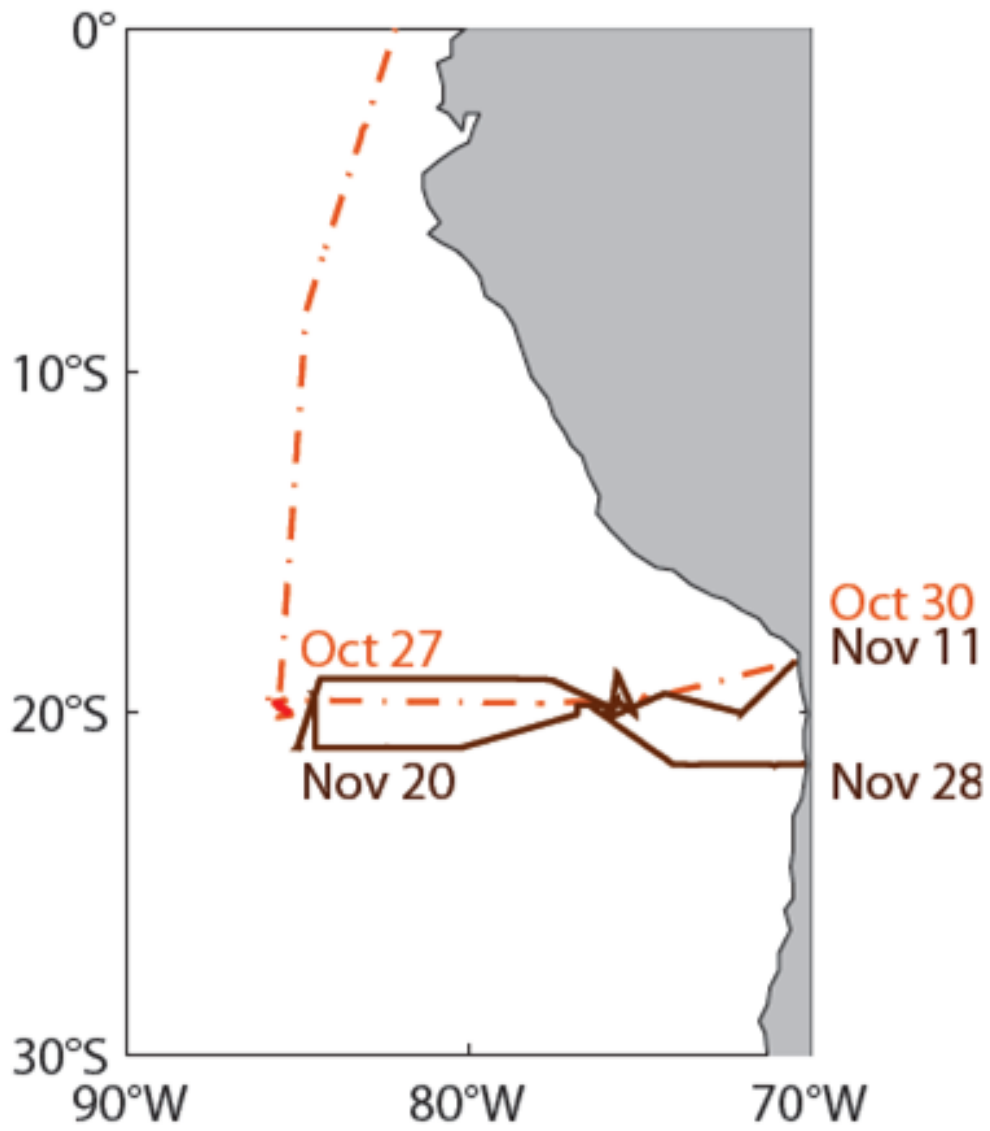


Figure 2.1: Path of the NOAA Research Vessel RHB during VOCALS (brown solid line).

Data used in this study is all data west of 75 °W. Image courtesy of Simon de Szoeke.

Chapter 3

Methodology

3.1 Precipitation Core Identification

Regions of strong precipitation represent an avenue to remove moisture from the cloud layer and therefore potentially aid in breaking up cloud cover (Berner 2011). To this end, we seek to understand and isolate the properties of the stratocumulus precipitation in this region. The first step is to identify precipitation cores, defined here as regions of precipitating stratocumulus that produce enough drizzle, across a large enough region, to be confident that precipitation is reaching the ocean surface for a sustained period (Comstock et al. 2005).

These regions represent localized concentrations of liquid water path (LWP) of 300 g m^{-2} and greater (Comstock 2004). The identification of strong precipitation cells is done using the cloud base radar reflectivity from the C-band radar (Figure 3.1 a,b). In order to isolate the precipitation that is reaching the surface and therefore contributing to water flux out of the cloud layer, a radar reflectivity threshold was applied to the field where all values less than the threshold are removed from the image. A threshold filter of 5 dBZ is used to remove regions of weaker regions of echo, including sea clutter near the radar, and to limit the analysis to precipitation that is reaching the surface with minimum rain rates of 0.1 mm hr^{-1} (Comstock 2004). Precipitation reaching the surface acts as a sink for water in the

atmosphere. Reflectivity values lower than 5 dBZ are likely to be precipitating at a rate ($< 0.1 \text{ mm hr}^{-1}$) such that a large portion of the liquid water is evaporated before it reaches the surface (Comstock et al. 2005).

3.2 Feature Detection

After the threshold filtering was applied, cell detection (aka feature detection) was performed on the radar reflectivity data from each radar scan. Precipitation cores are identified by finding regions where pixels are connected using any of their 8 neighbors (Haralick and Shapiro 1992). Each locally isolated, contiguous region is labeled with a unique identifier corresponding to its frame (individual radar volume and time) and latitude and longitude location (Figure 3.1c) . With the goal of detecting only significant precipitation cores, the following thresholds were used:

- 1) Intensity threshold greater than or equal to 5 dBZ
- 2) Area threshold greater than or equal to 1 km^2
- 3) Core centroid is at least 8 km from center of the radar domain and no closer than 5 km from the maximum range

A precipitation core size threshold of 1 km^2 was used to represent cores that have a significant precipitation area. This minimum size corresponds to the “well behaved” portion

of trade-wind cumulus precipitation during RICO (Trivej and Stevens 2010). Trivej and Stevens showed that cells between 1 and 10 km² followed log-normal distributions which are consistent with previous work on cloud size distributions (Lovejoy 1982) and distributions of radar echo size (Lopez 1976, Houze and Cheng 1977, Holder et al 2008). Cells significantly larger than 10 km² show a smooth, predictable trend away from the power law approximation, while cells smaller than 1 km² are not as well described. In terms of the radar data used in this study this limits the definition to cells that have a contiguous arrangement of 16 pixels or more (Figure 3.1 d).

Lastly, a location based filter was also applied in order to remove the effects of range, both near the radar and at maximum range, from contaminating core intensity distributions. Cores whose centroid was closer than 8 km to the center of the radar domain or 5 km from the maximum radius of the radar were removed. This removes cells whose lifecycles are only partially in the domain and therefore partially unobserved (Figure 3.1 d).

The result of the filtering and thresholding is that about 75 % of the regional precipitation is accounted for in this study. This increases to 90% or greater during heavy rain periods. The portion that is filtered out is the very light drizzle that is likely to evaporate just below the cloud layer.

3.3 Tracking Method

Once the precipitation cores are identified, they are connected temporally using an extension of standard centroid-to-centroid tracking (Dixon and Weiner 1993). One significant advantage of this data set is that the radar volumes are completed every three minutes instead of every 6-10 common to operational National Weather Service (NWS) Weather Service Radar (WSR-88D). This means that a precipitation core that experiences a 20 minute lifecycle would appear in 6-7 frames in our data versus 2-3 in the NWS operational data set. The centroid, size, and shape of each cell are used to determine which cell in the next frame is most likely the future version of the original. Previous methods (Dixon and Weiner 1993, Johnson et al 1998) use a centroid-to-centroid projection technique that requires that the reflectivity weighted centroid of the future track lies within the predicted region of advection. This is nearly always the case for high local maxima storm systems (i.e. strong convective cores, hail, etc) but this is not necessarily the case where the spatial gradients of reflectivity are weak and cell mergers and splits happen rapidly. Lakshmanan et al (2009) used a method that also includes the cell area as a consideration but broke “ties” by maximizing track length, which again favors intense events. Rather than connecting a centroid to a future centroid, my method connects the entire precipitation core (entire region above dBZ threshold) to another core.

Internally to the algorithm, the shape and size of original cell is simplified as an ‘abstracted cell’ consisting of a multivariate normal distribution in the shape of an ellipse where one axis is proportional to the size of the original cell in the direction perpendicular to the track’s movement direction, and the other axis of the simplified cell is proportional to the size of the cell in the flow-parallel direction (Figure 3.2). The cell’s corresponding multivariate normal distribution has a covariance matrix (eqn. 1) equal to the product of the original cell’s covariance matrix and a weighting function that can be used to customize the process for various conditions.

$$\text{Covariance Matrix} \quad \Sigma = \begin{bmatrix} C_{\perp} * W_{\perp} & S \\ S & C_{\parallel} * W_{\parallel} \end{bmatrix} \quad (1)$$

Where C_{\perp} is the variance in the advection-parallel direction, C_{\parallel} is the variance in the advection-perpendicular direction, S is the covariance of the two axes (the skew) and W_{\perp} and W_{\parallel} are weighting parameters. This method insures that tightly organized cells whose perimeters are smooth have prediction distributions that are more concise, while cells that show significant roughness around the perimeter are given more flexibility in their future configuration. This simplified, abstracted version of the original cell represents a middle ground of the most likely shapes and orientations of the future cell. The weighting function included in the algorithm is an attempt to better account for complex, evolving cells or cells that are moving in a direction significantly (> 20 degrees) different from what is expected based on prevailing wind speed and direction and acts to broaden the predicted distribution in the advection-parallel and/or advection-perpendicular directions.

This method allows for a field where each cell can have significantly different local maxima from other cells in the field and still be tracked using the same algorithm. The previous methods (Dixon and Weiner 1993, Johnson et al 1998, Lakshaman et al 2009) were designed for a field where 5-10 clear local maxima were to be tracked, all of which were roughly the same intensity as each other and were of intensities (30-35+ dBZ) far above the background levels. This algorithm can handle 60+ simultaneous cells that are both very close in local proximity and of significantly different intensities. An anecdotal comparison can be made to how a fisherman casts a net at a school of fish. The rough size of the net can be restricted or expanded based on the apparent size of the school at the time of casting. Once the net leaves the fisherman's hands its size and shape are fixed and it proceeds towards where the school was swimming. It's unlikely that the fish school will change size, shape, and direction significantly in the time it takes for the net to fall into the water and so as long as those three variables are mostly preserved, the cast will be successful.

Abstracted cells from one frame are projected forward in space using an advection speed and direction that is held constant. If winds vary gradually from one frame to another the median advection of the recently tracked cells can be used to help guide the forward projection (as is the case for marine stratocumulus in the Southeast Pacific). In the case of synoptic systems that experience large wind shifts coupled with moderate variations in speed and advection direction throughout their lifecycle, a workable solution would likely be to determine, a priori, the approximate advection and couple this with the frame-to-frame guidance provided by the algorithm to track smaller precipitation features within the larger system.

No continuous, direct measurement of cloud level winds exists for this data set, but observations from radiosondes and visual inspection of radar show that winds vary between about 8-12 m/s and by only about ± 20 degrees in direction (de Szoeki 2010). These variations correspond to about a 1 pixel error from constant advection between 3 minute radar frames. A method was developed to allow for varying rates of cell advection by taking the median advection rate of the previous frame's cells and no significant difference in tracks was found. The algorithm also removes from each frame the ship displacement before projecting the cells future location. This ship displacement was removed because it represented a 3-4 pixel error in the projected location of the cell, significantly greater than that which occurs simply from changes in advection. For this study a constant 10 m/s advection speed was used with a fixed advection direction towards 310 degrees azimuth (winds are from 130 degrees). This translates to an image advection speed of approximately seven pixels (± 1 pixel) between 3 min radar frames. The algorithm is designed with sufficient flexibility and robustness to overcome the complications inherent with this set of data.

With the abstracted cell translated forward in space, any real future cell that has a portion underneath the abstracted cell is marked as a potential connection. For each pixel in a future cell underneath the translated past cell, the value of the normal distribution is recorded at that location. After the value for each pixel in the future cell is found, the sum of those values becomes the cell's score with regard to that specific potential parent cell. Therefore, each past (parent) cell is allowed to potentially connect to any future cell, and for each future cell

that is partially underneath the translated parent cell, the cell that has the highest score (above a minimum threshold) is connected. In the case where two parent cells connect to the same future cell, the parent cell to which the future cell scores highest is connected. The goal of this procedure is that the cell that is most similar in size, shape, and estimated future location to the previous cell is connected as a track.

The algorithm assigns a new track to a cell when it first appears and ends a track if no cell is caught by the parent cell above a sufficient score. This can occur for cells that don't have a future cell to connect to (or that are out scored by a better matched cell). Cells in the region frequently merge together, in which case the cell track that didn't win is ended. A similar treatment is made for cells that split from one large cell to two, or more, smaller cells causing the larger cell to retain the original track and the smaller cell to get a new unique track. There are several potential problems when trying to track features in a real-world, variable field. Primarily the number, size, and intensity of cells can change significantly between frames. The algorithm is extremely flexible regarding size and intensity changes as long as they do not fall below the thresholds outlined above.

The total precipitation volume for echoes with reflectivities greater than 5 dBZ observed during the VOCALS cruises is $7.18 \times 10^7 \text{ m}^3$. Seventy percent of this volume is accounted for by 9630 tracked cells that are > 5 dBZ, have an area > 1 km^2 , and have tracks longer than 15 min. Tracks that last fewer than 15 minutes (5 frames) are not considered in the track statistics portion of this work as they do not have enough data points to form conclusions about lifecycle. An additional filtering step is required since tracks truncate when cells move

out of the radar domain or across the cone of silence over the radar. So as to not include these artificially shortened tracks in our statistics, we remove tracks near the edge of the radar domain and the cone of silence. After this final filtering, 4,532 tracked cells remain. We assume that the location of the cell relative to the ship has no impact on the individual cell's behavior. The 4,532 tracked cells remaining account for $2.12 \times 10^7 \text{ m}^3$ of rain volume > 5 dBZ (30% of rain volume for echoes > 5 dBZ). The characteristics of the cells along each track can be mined for information about how the cell evolves over the course of its life. Cell intensity (mean, median, max, and distributions of dBZ values), cell size, and other parameters were examined over the lifetime of the cell to determine if there are patterns of changes that occur in multiple cells or commonality with other variables. The duration of the cell track is used to group cells with similar lifetimes.

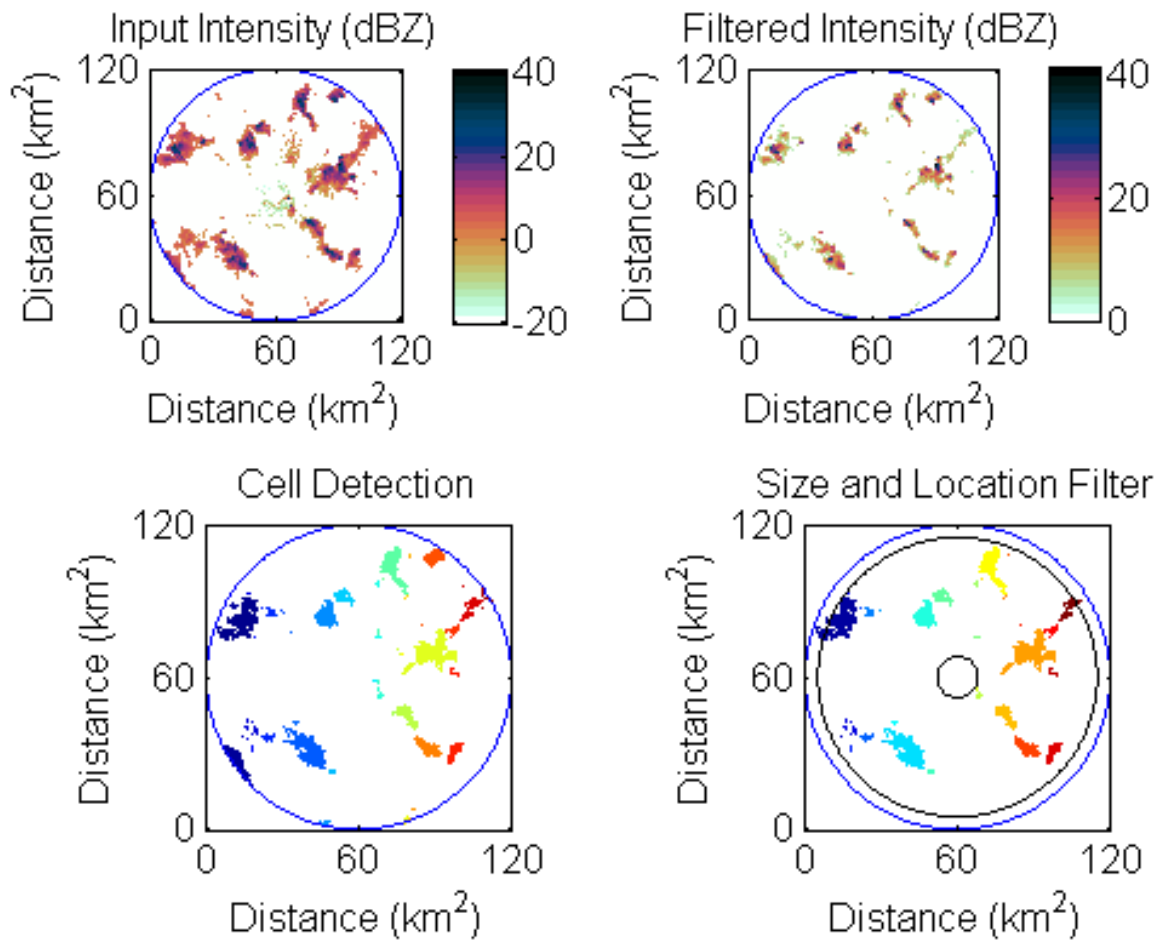


Figure 3.1: Step-by-step example of filtering process. (a) The original intensity recorded from the C-band radar. (b) After removing echo below 5 dBZ. (c) Each contiguous region is given a different color corresponding to a unique identifier. (d) Regions smaller than 1km² and regions close to range limit or center of the domain are removed. All regions have the outer range limit of the radar shown as a blue circle and (d) has two black circles drawn to show the regions from where cell centroids were removed.

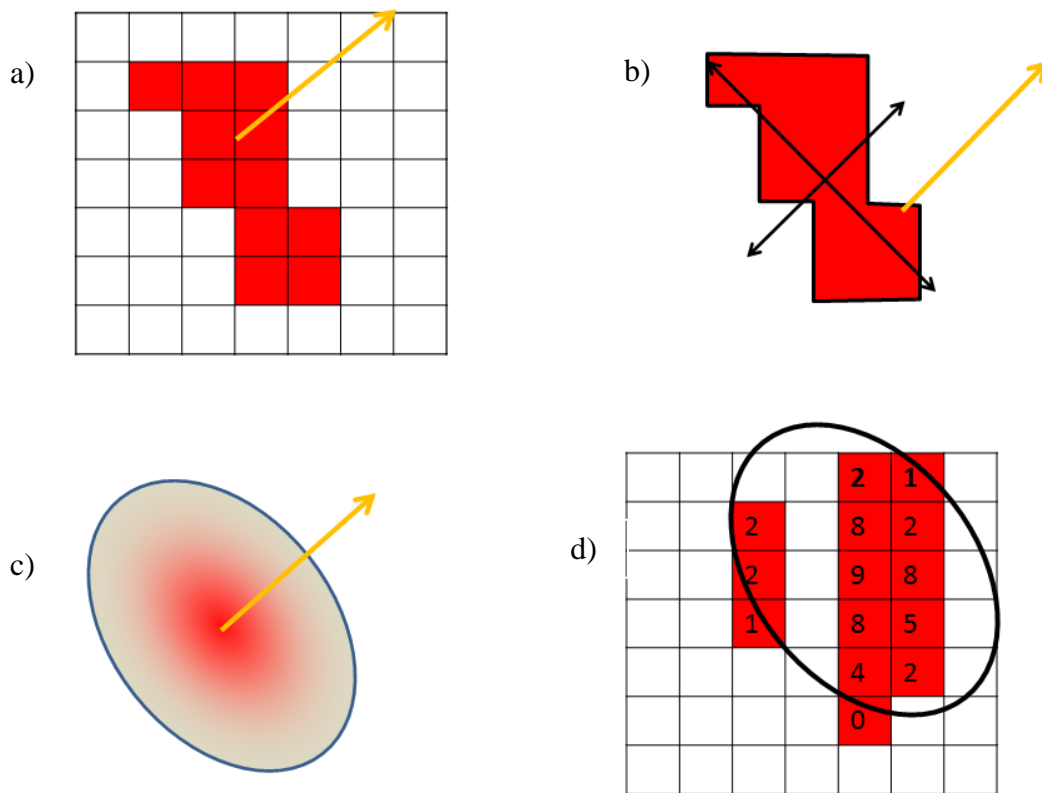


Figure 3.2: Simplified example of the four main steps involved in the feature tracking algorithm. (a) Identify the cell and its direction of travel (orange arrows). (b) Determine the variance of the cell in the advection-parallel and advection-perpendicular directions (black arrows). (c) Replace cell with a multivariate normal distribution with covariance described in eqn. 1. (d) Advect abstracted cell, scoring the next time's features that occur under the abstracted cell based on the value of the normal distribution at that point.

Chapter 4

Results

4.1 Data Set Statistics

Of the 31 days of data collection by the ship, a little more than 21 days of radar data were obtained in the stratocumulus region south of 15° S and west of 75° W. Of these 521 hours, 483.5 hours also had an associated cloud fraction estimate from the satellite data which break down as shown in Figure 4.1. The satellite data was missing for the remaining 37.5 hours. The ship was in overcast conditions for 257.25 hours, representing just over half (53%) the sample period. During the overnight period, broken (32.85 hrs), transition (23.9 hrs), and scattered (33.65 hrs) or less were observed roughly equally while during the day the transition periods were only rarely observed (11.8 hrs). During the day the second most common cloud fraction was scattered or less (73.2 hrs) which was observed only slightly less frequently than daytime overcast (100.9 hrs).

Figure 4.2 shows the average number of radar precipitation cores per hour during each of the four different observed cloud conditions in the 120 km diameter radar,. The times shown represent the four hour sampling windows of the GOES IR satellite data used in this study. The number of precipitation cores varies with the strong diurnal modulation of precipitation

and cloud fraction (Burleyson et al. 2013), with some differences noticeable between cloud conditions. Burleyson et al. (2013) analyzed precipitation core frequency related to the diurnal cycle alone, and found that precipitation cores were maximized overnight and minimized during the day. When core frequency is conditioned on both the diurnal cycle and local cloud fraction a slight refinement can be made. All three cloud conditions show an increased number of cores overnight compared to daytime, but the overcast cloud condition showed a more rapid response, in number of cells, after the sun sets than the non-overcast conditions. The number of precipitation cores in overcast conditions increases from a minimum of 8.5 cores per hour during the midday period (1100 – 1500) to 16.5 cores between 1500 – 1900, and then to a plateau of 21.5 – 22.5 between 1900 – 0700. During this same period the number of cores per hour in broken cloudiness increases from 2 during midday to only 9 by the 1900 – 2300 period. However, while the overcast conditions averages more cores earlier in the evening, the average number of cores per hour in broken conditions continues to increase to 28 (2300 – 0300) and to a peak of 30.5 by the earlier morning (0300 – 0700). The increase in scattered conditions was delayed even more than broken conditions, averaging between 6 and 8 cores per hour from midday to 0300 and reaching a maximum of 21 cores per hour between just before sunrise (0300 – 0700).

The different cloud conditions also experienced different cell count amounts when comparing at the across the same time of day. During the late overnight hours (2300 – 0600), when precipitation is maximized for all conditions, the broken and transition regions saw an average of 30 precipitation cores per hour. This is 36 percent greater than the 22

precipitation cores per hour in the overcast conditions. However, for the late afternoon observations (1100 – 1800) overcast conditions averaged 12.5 cores per hour and the broken and transition regions averaged only 5 cores per hour. Scattered or less conditions showed fewer cells on average than any other regime, having the fewest cells for all hours except 1100 – 1800.

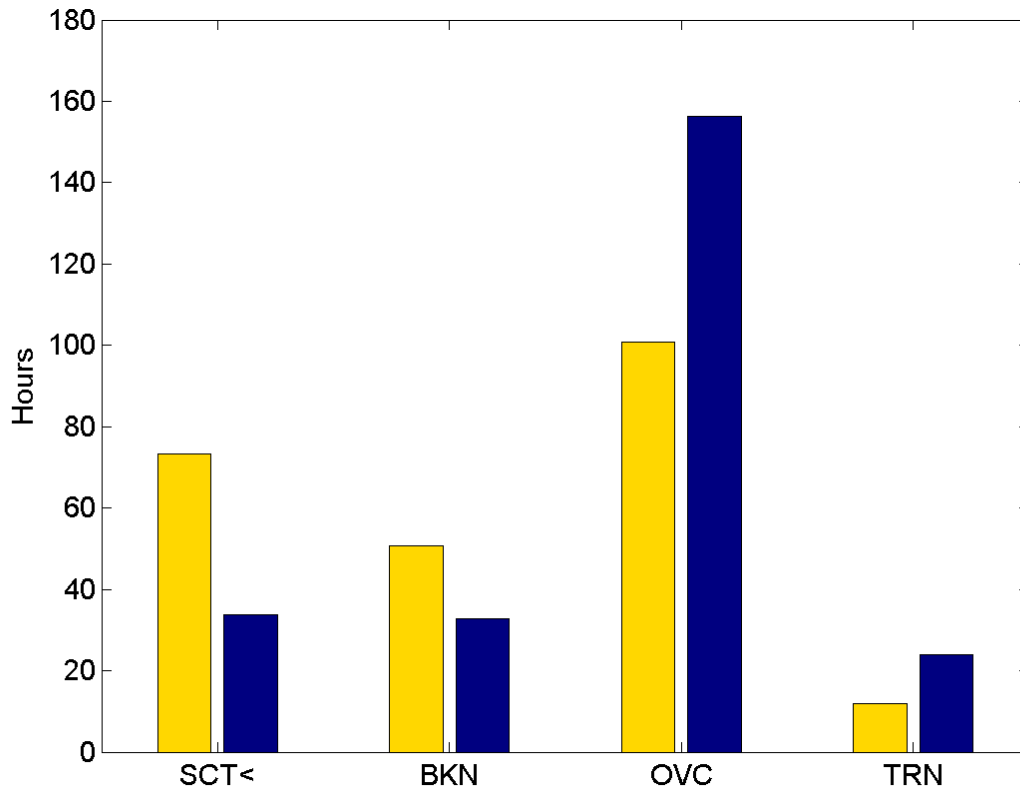


Figure 4.1: GOES IR observed sky condition within the 120 km radar domain during the VOCALS-Rex cruise. Number of hours are shown for each cloud conditions, separated into day (0600 – 1800 local) and night (1800 – 0600 local) as indicated by the blue and yellow respectively.

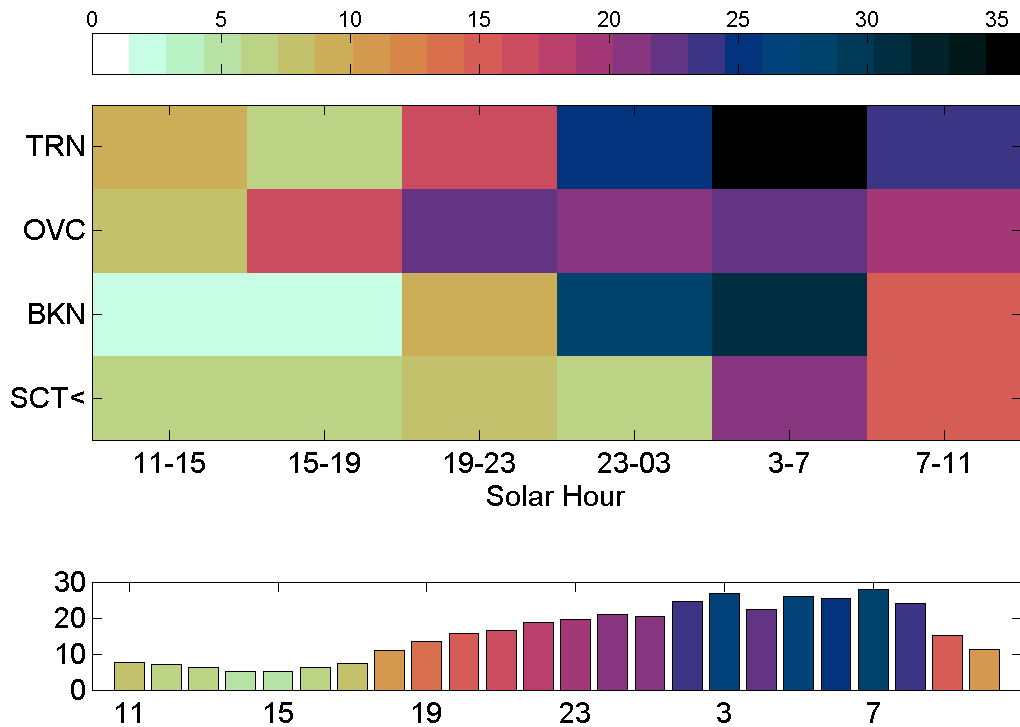


Figure 4.2: Average number of precipitation cores (see methodology) (top) observed for each period and sky condition and (bottom) for each hour with the sky conditions combined. This number represents the average number of cores within the 120 km radar observation diameter at any moment during each solar hour and each cloud condition.

4.2 Bulk Track Statistics

Automated tracking of cells provides the opportunity to examine the ordered time sequence of individual cell characteristics, illuminating the overall cell behavior. The aggregate cell behaviors can be examined to examine the nature and variability of drizzle cell evolution. Shown in Figures 4.3, 4.4, and 4.5 are some examples of a few of the longer tracks in the data set. Each figure features a set of three radar frames from near the beginning and at roughly one third and two thirds along the cell's track. Also shown is the evolution of both max intensity and size. The peak intensity of the cell would be the maximum value obtained in the green line. Additionally, a histogram of the intensity distribution inside the cell is shown for each time along the track. Figures 4.3, 4.4, and 4.5 show a distinct intensification/dissipation cycle similar to that observed in previous work in the Southeast Pacific (Comstock et al 2007). Figure 4.3 shows a reasonably typical cell that reaches a peak intensity (21 dBZ) in the median range (Figure 4.6). The cell does not change significantly in area over its life and dissipates after 42 minutes. Figures 4.4 and 4.5 show some examples of other features observed in the tracks. Pulsing is evident in Figure 4.4 with the cell not changing significantly in size, but experiencing a peak intensity change of 15 dB twice over its observed life. Figure 4.5 shows an example of a cell that has slightly smaller fluctuations in intensity but experiences a significant growth after 60 minutes of relative constant size from about 5 km² to more than 40 km². In this case, the cell was isolated and its rapid growth was not from mergers with nearby cells (Figure 4.5 a,b,c), but internal growth by increasing cell radius.

Figure 4.6 shows the distribution of speeds and travel directions for 1493 cells with tracks longer than 30 min. The travel direction of the precipitation cells in this region is very close to the average prevailing wind direction (towards 310) with very little overall variability. Cell advection speeds are also in-line with wind speeds in the region, with the majority of cells having a ground relative speed between 6 and 10 m/s.

For this analysis, we are looking at three main characteristics that define the overall intensity of each core's lifecycle: peak cell maximum (peak intensity), median area, and duration (Figure 4.7 and 4.8). We also examined several criteria used to compare against prior work including median cell maxima, maximum area attained during each cell's lifecycle, and the fractional contribution to the total precipitation area for different cell size ranges. For the purpose of this work, statistics that are dependent on the ordered sequences of track-based observations will be referred to as "behaviors", while those that are not based on tracked data will be referred to as "characteristics". The tracking algorithm identified 4,532 tracks that are at least 15 minutes in duration. The peak intensity is defined as the single highest recorded value (dBZ) during the cell's life. Median track intensity is the median of the maximum intensity values measured for each recorded frame of the cell's lifecycle. Max obtained area is the highest recorded area value during the cell's life. Median area is the median value of precipitation core size during the entire track. Duration is the length that the core lasted before dissipation or merging with another cell. Of the tracks longer than 15 minutes, approximately 27 percent are longer than 30 minutes and approximately 1 percent are longer than 90 minutes. The median duration is 21-24 minutes. Herein, the 85th

percentile is used as a representation of the upper portion of the distribution of the different cell statistics. Figure 4.7 shows the distributions of max intensity, median intensity, median area, duration and max area obtained for all tracks longer than 15 minutes.

The frequency and cumulative distributions of track behaviors (Figure 4.7) all show strong positive skew with comparatively low modal values. An empirical fit of the cumulative frequency of peak intensity with a log-normal distribution with $\mu = 2.933$ and $\sigma = 0.012$ yields an extremely good fit. The median area and area are not log-normal, but do exhibit some exponential-like qualities.

Figure 4.9 shows joint frequency distributions of peak intensity versus duration and median area. A clear association among the peak intensity, median area, and duration can be seen. A tracked cell with higher peak intensity, on average, is more likely to be larger and longer lived than a cell with weaker peak intensity. The conditional probabilities indicate that for cells smaller than the 85th percentile of area, only 1 in 11 (9 %) tracks reach a peak intensity above 26.5 dBZ. However, when looking at cells greater than the 85th percentile of area, 1 in 2 (50 %) of the tracks exceeded 26.5 dBZ.

A Venn diagram nicely shows the interrelationships among the three track behaviors (Figure 4.10). The ratios of values in the Venn diagram are analogous to a conditional Bayesian statistic. Given a cell exhibiting one type of behavior, the likelihood of it exhibiting another can be approximated by the ratio of the number of observations of the two. Thirty percent

(1369 tracks) of all tracks exhibited one or more behaviors at or above the 85th percentile. Of the 680 cells that were at or above the 85th percentile in intensity (26.5 dBZ), 458 (67 %) are also in the 85th percentile for either area, duration or both. This relationship holds for the other two behaviors, though slightly weaker. Given that a cell is in the 85th percentile of area (9.4 km²), 68 percent of the time it will also be above the 85th percentile in intensity and/or duration. Given that a cell is long lived (≥ 42 minutes), 52 percent of the time it will also be very intense or very large. Lastly, there were 171 cells that were at or above the 85th percentile in all three variables representing approximately 12 percent of the tracks in the Venn diagram and 4 percent of the total observed tracks.

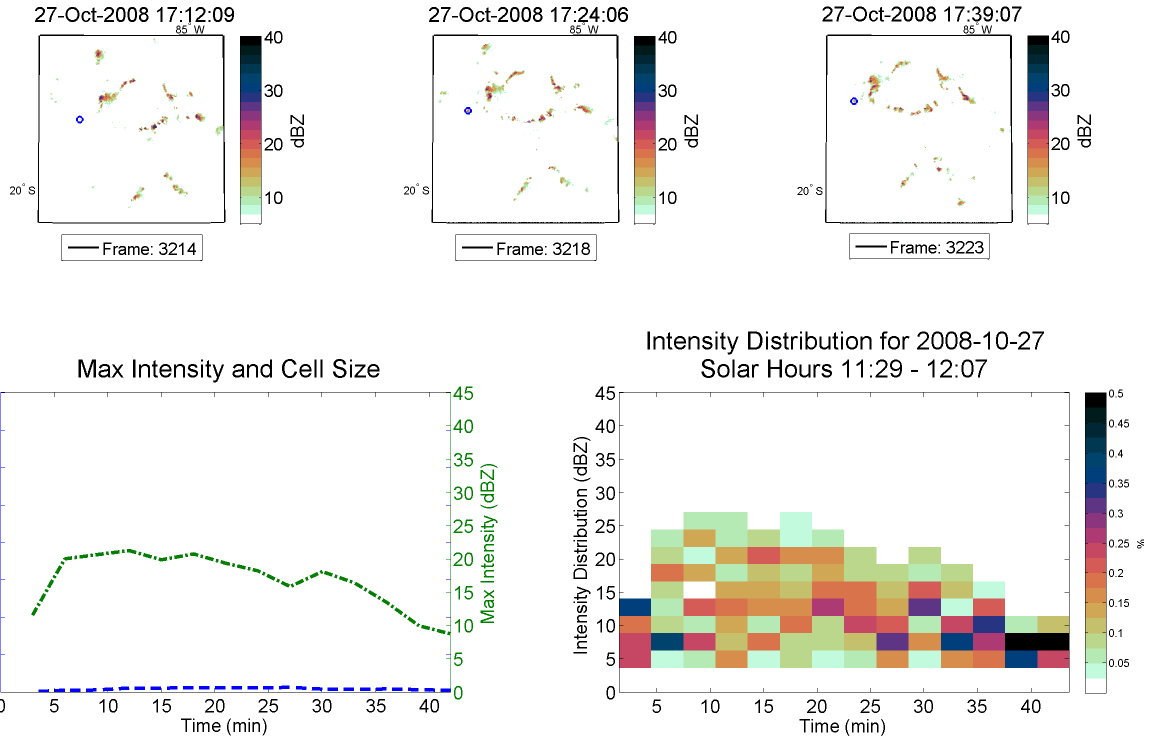


Figure 4.3: Track overview for a sample track occurring on 27 Oct 2008 at 17:12 UTC. Top three frames show sample radar frames during the lifetime of the cell with the cell highlighted in the blue circle. Bottom left is the cell size (blue) and max intensity (green) inside the cell during each observed time. Bottom right is the distribution of intensities inside the cell for each observed time. Time is given in minutes since the beginning of the track.

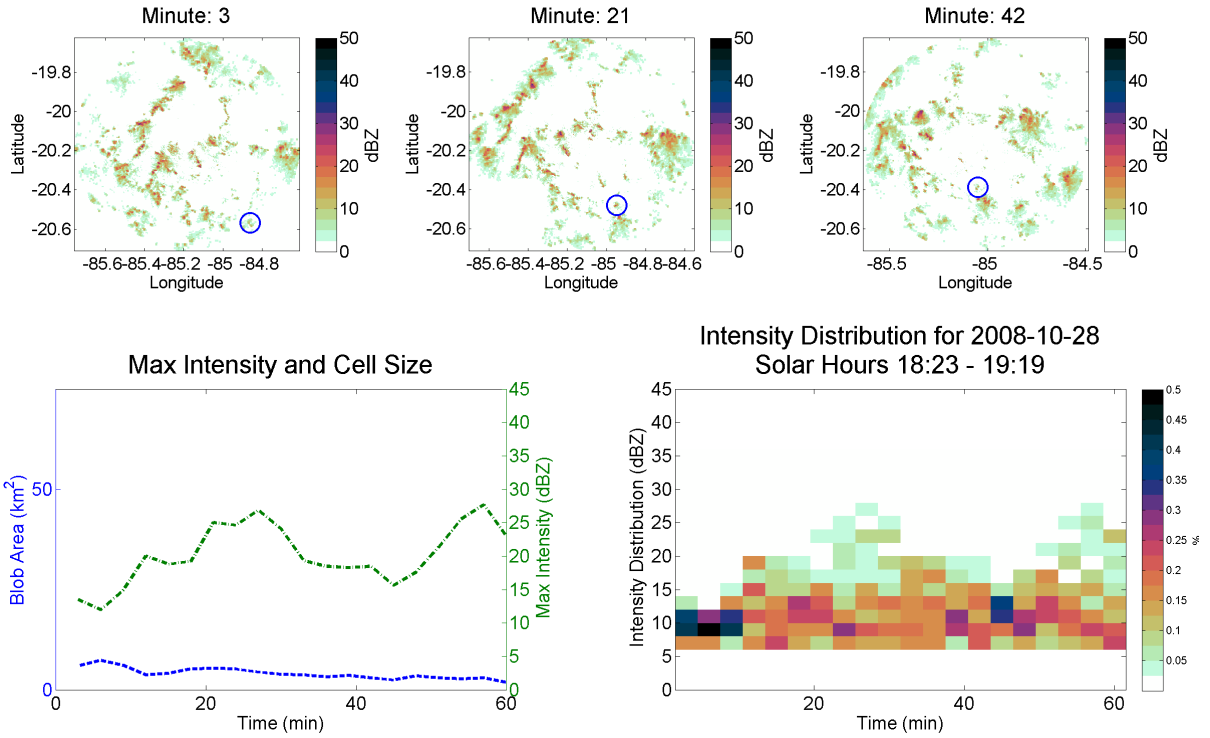


Figure 4.4: Track overview for a sample track occurring on 28 Oct 2008 at 23:06 UTC. Top three frames show sample radar frames during the lifetime of the cell with the cell highlighted in the blue circle. Bottom left is the cell size (blue) and max intensity (green) inside the cell during each observed time. Bottom right is the distribution of intensities inside the cell for each observed time. Time is given in minutes since the beginning of the track.

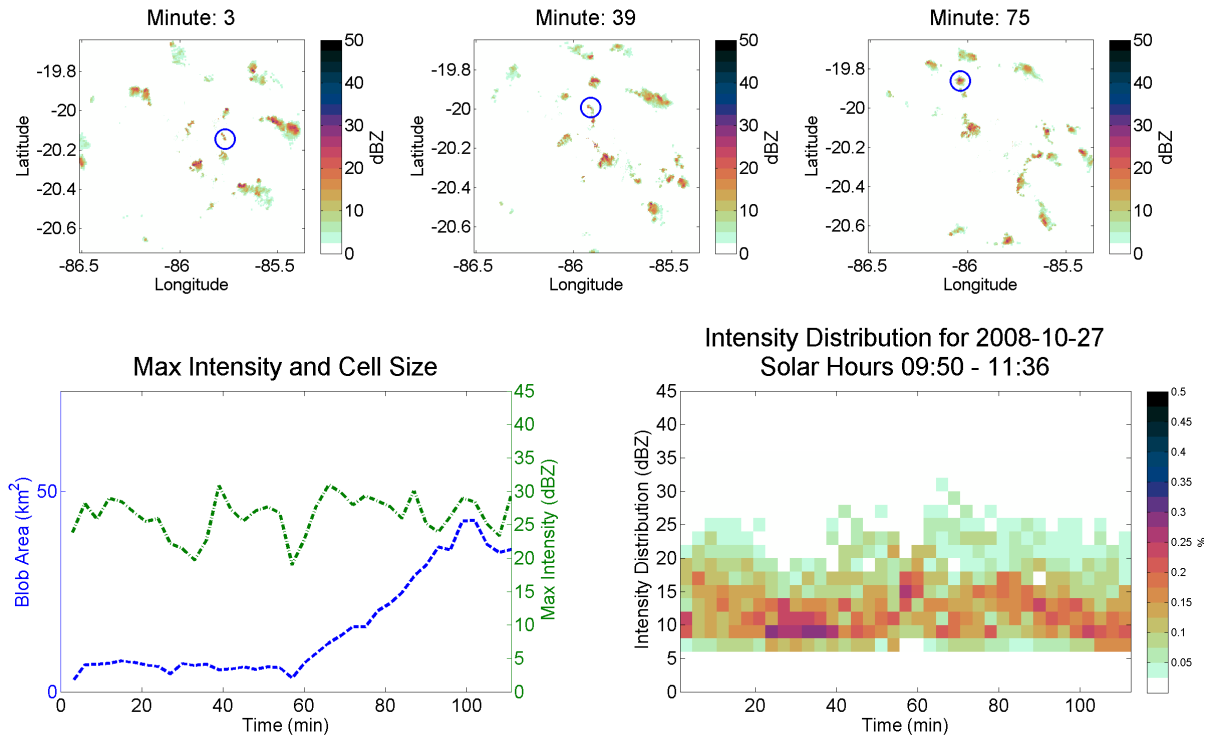


Figure 4.5: Track overview for a sample track occurring on 27 Oct 2008 at 14:33 UTC. Top three frames show sample radar frames during the lifetime of the cell with the cell highlighted in the blue circle. Bottom left is the cell size (blue) and max intensity (green) inside the cell during each observed time. Bottom right is the distribution of intensities inside the cell for each observed time. Time is given in minutes since the beginning of the track.

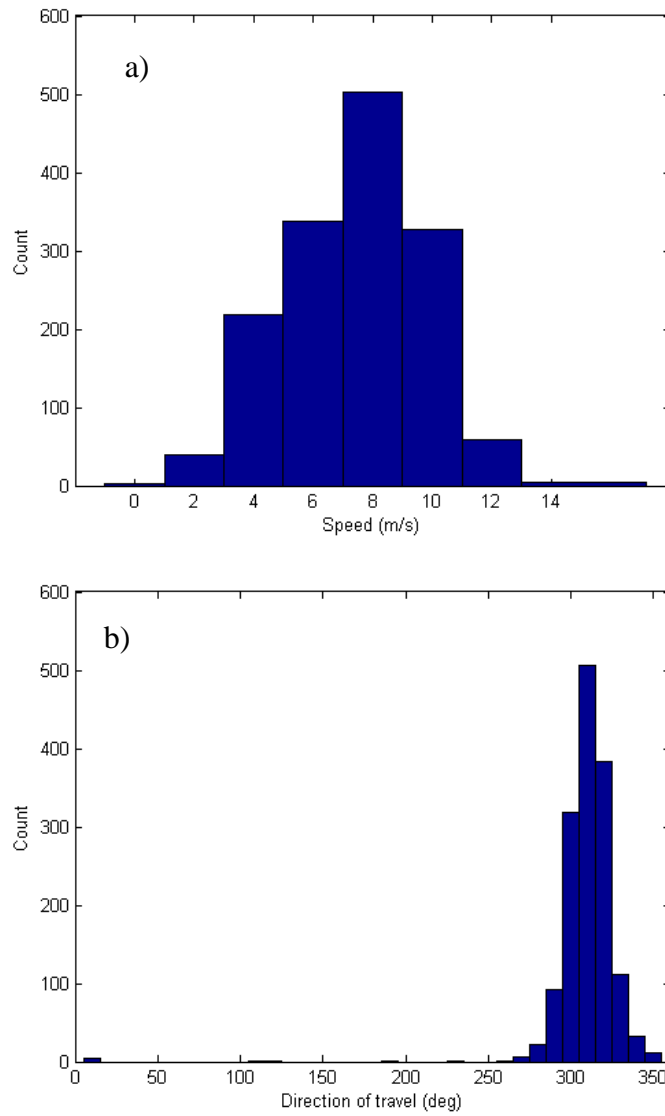


Figure 4.6: Track velocity (a) and track travel direction (b) for all tracks 30 minutes or greater. Both values use the first and last points to best capture average values.

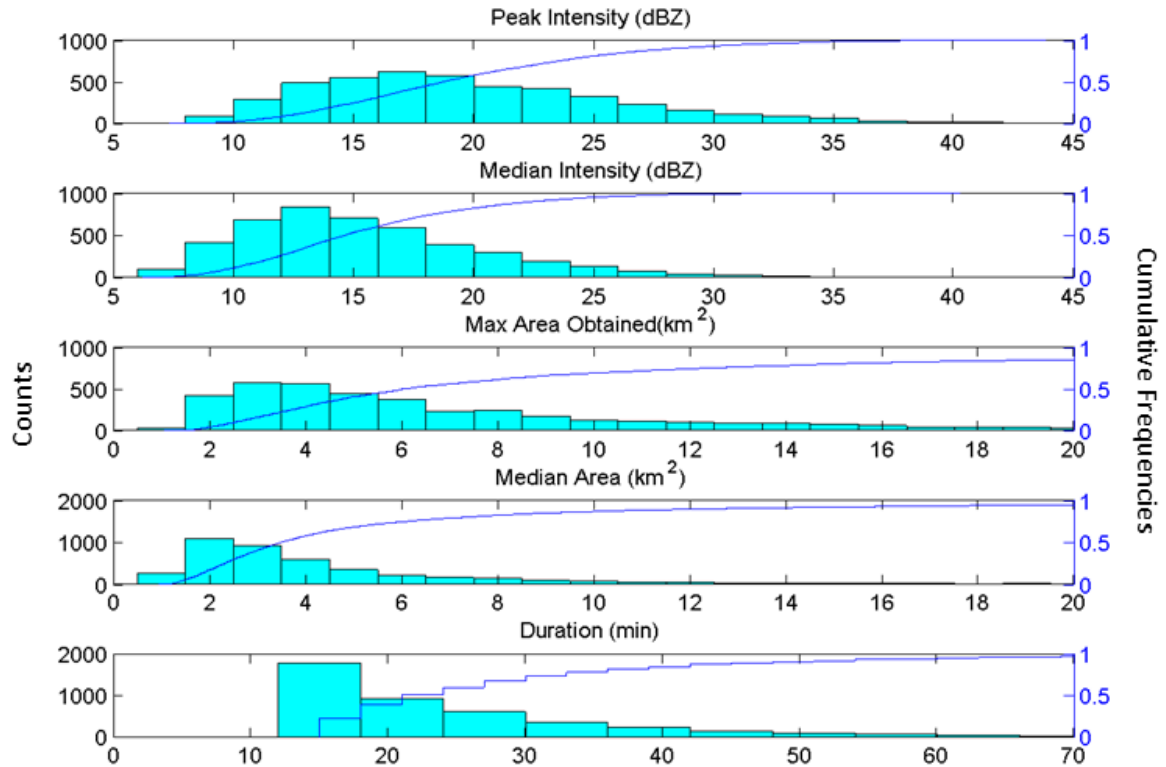


Figure 4.7: Frequency (bars) and cumulative (line) distributions of peak intensity, median intensity, max area obtained, median area, and duration (top to bottom). The tails of the median area, max area, and duration distributions are cropped to better represent the bulk of the distribution. Duration appears discrete because each track's life time is always a multiple of 3 minutes due to the sampling frequency of the radar.

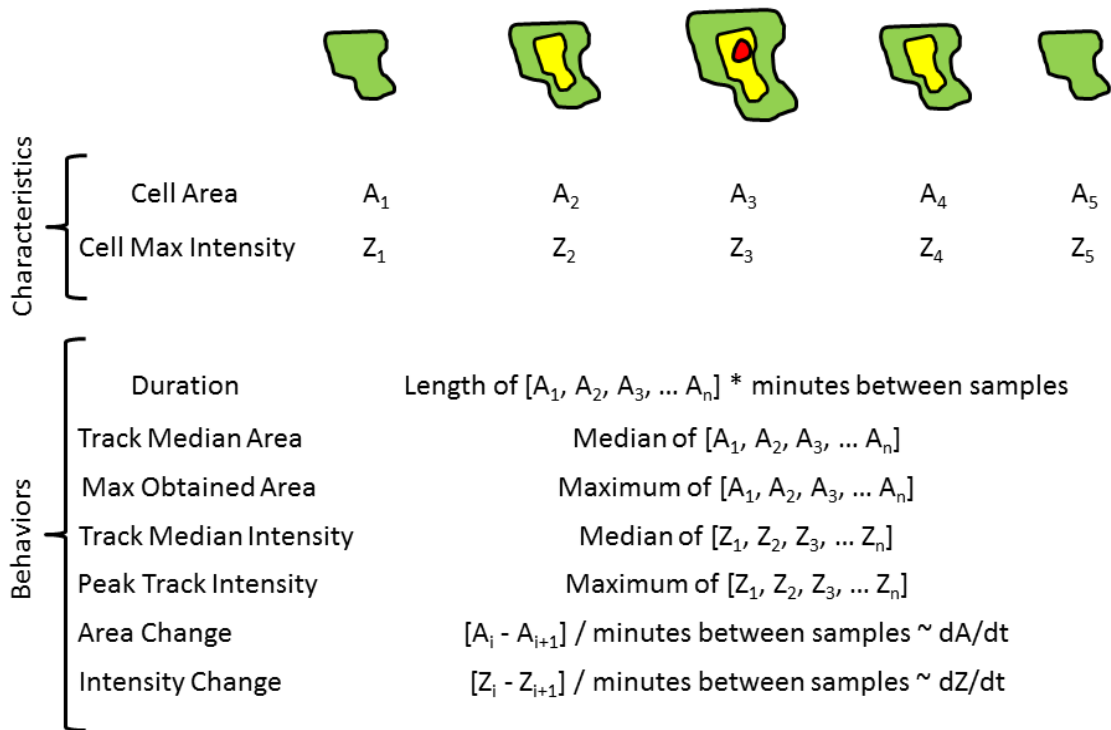


Figure 4.8: Summary of the cell characteristics and behaviors calculated for this work.

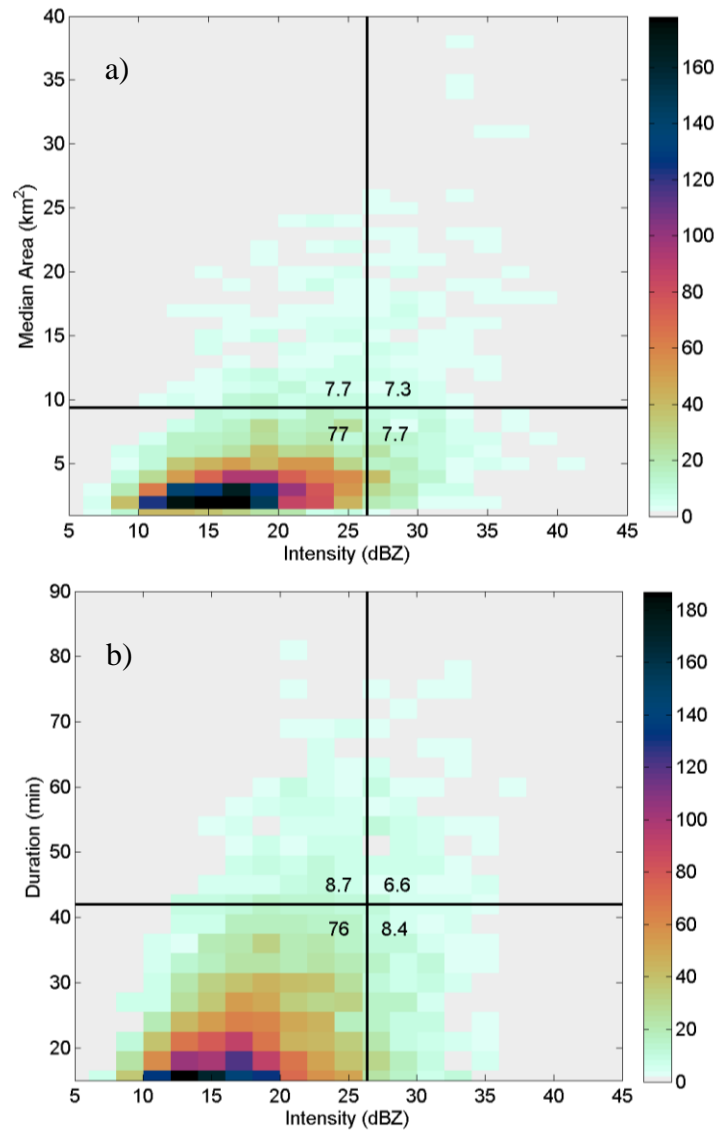


Figure 4.9: Distributions of peak cell intensity (a) versus median area and (b) versus duration. The 85th percentile of the distributions are shown as black lines, where vertical lines are intensity and horizontal are (a) median area or (b) duration. The number in each quadrant is the percentage of tracks that fall in the region bounded in the black lines.

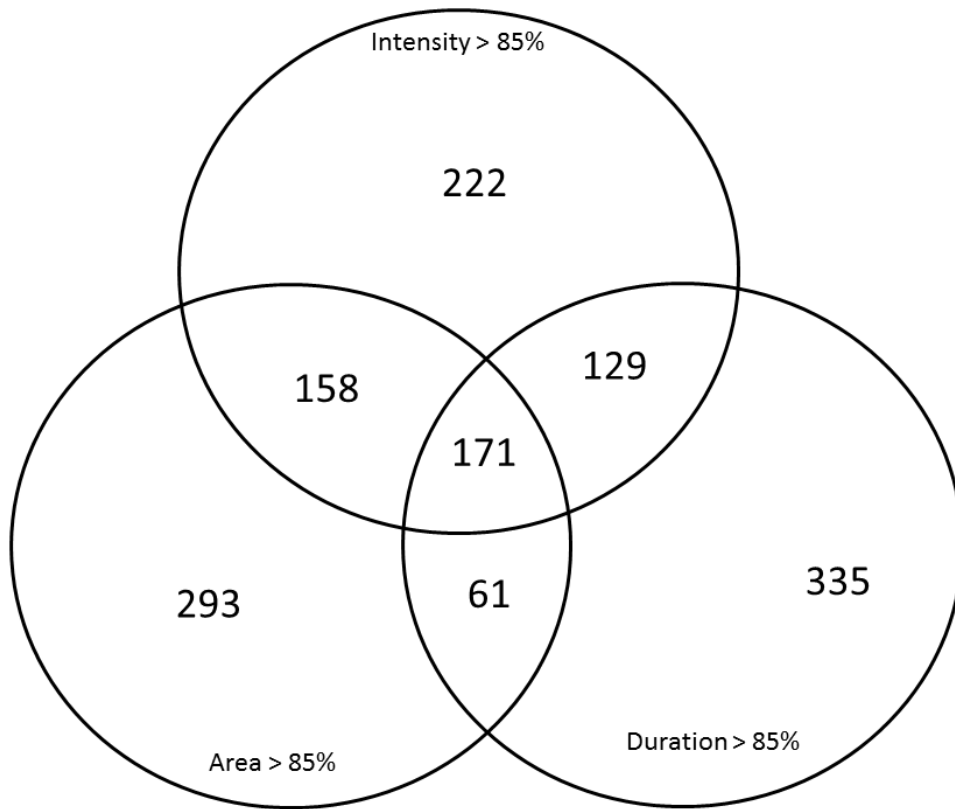


Figure 4.10: A Venn diagram of tracked cells with conditional behavior (among median area, peak intensity, and duration) at or above the 85th percentile. 680 tracks were at or above the 85% in intensity, 683 for median area, and 696 for duration.

4.3 Diurnal Cycle and Cloud Fraction

A primary forcing for this region is the diurnal cycle of shortwave radiation. This cycle causes changes in the cloud top radiative energy balance (Nicholls 1984, Betts 1990, Rogers et al 1995). These changes create significant amounts of turbulent mixing at and below the cloud top (Moeng et al. 1992, Bretherton and Wyant 1997). It has also been shown that both precipitation area and number of cells peak in the early morning, before sunrise (Burleyson et al 2013; their figure 8). The peak hours for number of drizzle cells occurs at approximately 2-4 AM local time and the peak for total drizzle area occurs slightly after this from about 3-5 AM local.

In general, the overnight hours (6pm – 6am solar hour) show a significantly higher number of precipitating cells (Figure 4.2) and total precipitating area (Burleyson et al 2013) compared to the day time hours (6am – 6pm solar hour). In addition to diurnal cycle, a further classification can be made by separating the cells into the cloudiness regime they occur in.

Figure 4.11 shows the peak intensity of each cell separated by cloud fraction and by time of day. The median of the distributions of peak intensity is relatively constrained across all 8 categories with a ± 1.25 dB deviation. In aggregate, the peak intensity of a cell is not a function of the diurnal cycle and therefore not a function of the number of cells or the cloud cover of the surrounding region.

Under overcast conditions, the most predominate condition, the distribution of intensities does not vary significantly with the diurnal cycle. In conditions other than overcast, sky condition and diurnal cycle together show some differences in the portion of the distribution above the 85th percentile. Under nighttime broken conditions, the 85th percentile of peak intensities was 8 dB greater (33 dBZ) than nighttime overcast conditions (25 dBZ). The median intensity during nighttime, broken conditions was also 2.5 dB greater than during nighttime, overcast conditions. The 85th percentile of peak intensity is lowest in overcast conditions (25 dBZ), with significantly higher intensities seen in the 85th percentile of transition (+4.5 dB), scattered (+2.5 dB) and broken (+8 dB).

The effects of the diurnal cycle on the region are further refined here. While overall precipitation is maximized overnight across all cloud conditions, the increase in precipitation overnight in overcast conditions occurs at least 4 hours earlier (1900 – 2200 LT) than in broken conditions (2300 – 0200 LT). Additionally, while stronger precipitation intensities are observed at night, the median intensities and typical development lifecycle appear very similar between day and night. The 21 days of VOCALS ship radar data support the idea that the most significant variable in terms of water budget is the number of precipitation cells (areal density of cells). While the number of cells is itself dependent on the diurnal cycle and cloud condition, the other parameters don't appear to be as effected and should therefore be considered secondary.

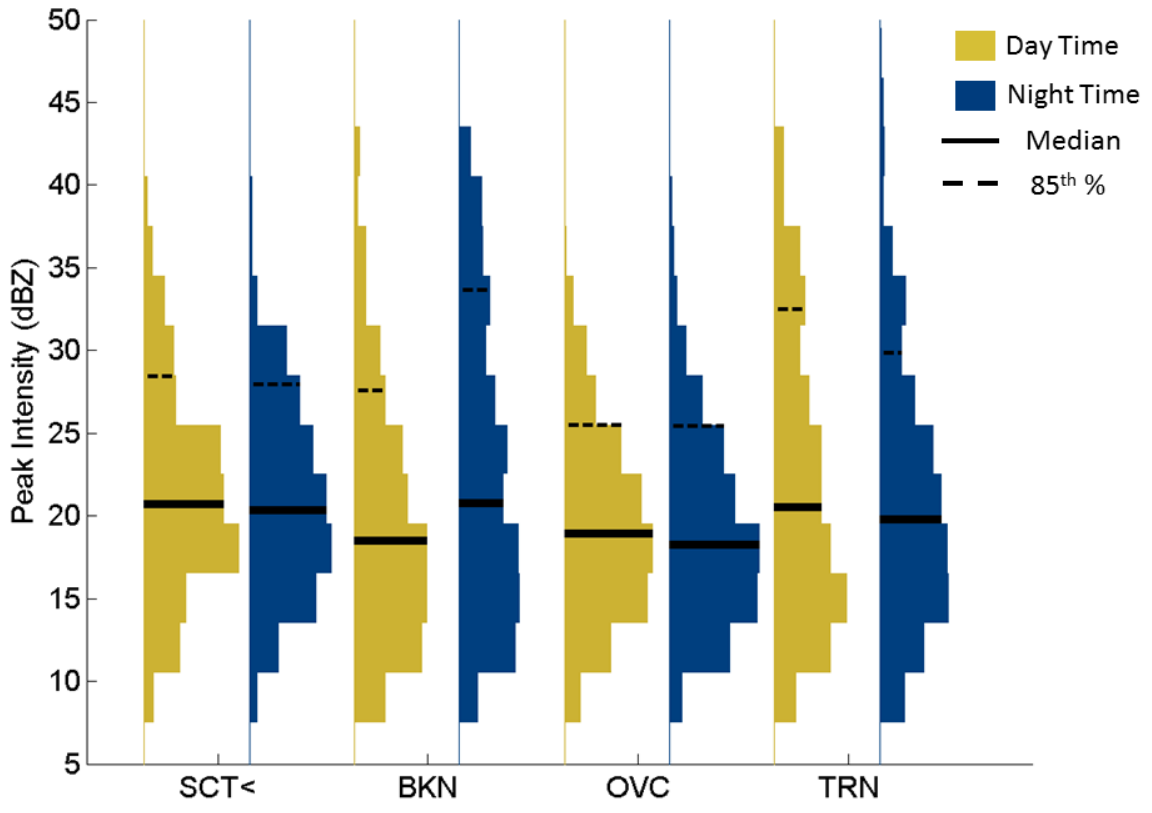


Figure 4.11: Distribution of peak intensities for the 4 sky conditions and 2 periods of the diurnal cycle. Median peak intensities are centered around 19.5 dBZ with a range of ± 1.25 dB. Outlier peak intensities of nocturnal cells are significantly larger for non-overcast skies than in overcast skies. The distributions are normalized by the number of cells in each category.

4.4 Cell Lifecycle

The set of tracks over 30 minutes long can be aggregated to look at modal changes over time of cell properties. Previous work on stratocumulus precipitation showed that a sample of hand-tracked cells experienced periods of growth and/or intensification followed by periods of shrinking and/or dissipation (Comstock 2005). The data set in this study offers a much larger collection of tracks to analyze. Figure 4.12 shows the change in max intensity over time for all tracks greater than 30 minutes. The temporal change (dBZ min^{-1}) has been filtered using a zero-phase, 3 frame filter in effect producing an average max intensity change per minute over a 9 minute window. During the first 30-40 minutes, the cells show intensification at a rate of $\sim 0.2 \text{ dBZ min}^{-1}$ for the first 20 minutes followed by dissipation period of 10 minutes at a rate of $\sim -0.2 \text{ dBZ min}^{-1}$. For the portion of cells that live longer than 30 minutes, the average dissipation rate is lessened overall (-0.05 to $-0.10 \text{ dBZ min}^{-1}$) with some positive values indicative of pulsing behavior shown in Figure 4.5.

To validate the observed intensification signal in the early part of the cell lifecycle and to clarify its interpretation, we will compare the cell developments of 118, 42-minute real cells against 10,000 42-minute simulated cells. The set of simulated cell tracks each reach their peak intensity at a random point during their lifecycle. The simulated cell tracks were created by picking the start, stop, and peak intensity from a randomly chosen real 42-minute track. The time-to-peak was chosen from a uniform random distribution between 3 and 39 minutes. The intensities along each simulated track linearly increase from start to peak and

then linearly decrease until the end of track. Ten thousand simulated tracks were created. Figure 4.13a and b compare the distributions of the rate of intensity change with time for the real and simulated 42-minute tracks and are computed using the same moving average, bin sizes, and dimensions. For the observed tracks, the median track behavior transitions from increasing to neutral at around 15 minutes (Fig.4.13a). In contrast for the simulated tracks (Fig. 4.13b), the median intensity transitions from increasing to neutral around the 20 minute mark, half way into the track. Since the simulated cells were allowed to reach peak intensity at any point during the track, about half the tracks are in a positive trend before 20 minutes and about half the tracks are in a negative trend after 20 minutes. For the observed tracks, the switch from mostly increasing tracks to mostly decreasing tracks occurs after 15 minutes instead of at the half-way point of track length. Additionally, this comparison also illustrates that the slow dissipation signal in the observed cells is robust since the linearly decreasing simulated cells have a sharper downward trend in intensity rate of change. While some tracks do experience intensification later in their lifecycle, it is clear that the most common behavior is for the strong intensification to occur over the first 15 minutes followed by slow dissipation until the cell dissipates.

The initial, rapid growth and slower dissipation is also evident in the temporal gradient of core area (Figure 4.14). Area increases early on as the cell experiences growth in size followed by a period of slow decline. These data suggest that what distinguishes long-lived cells (duration > 45 min) from shorter-lived cells (duration < 45 min) is that long-lived cells

can maintain themselves over 10's of minutes without significant change, reach slightly higher peak intensities, and take

The diurnal cycle, while modulating total number of cells, does not seem to effect the rate at which cells grow or dissipate. Figure 4.15 shows that the changes in intensity per unit time during the daytime and during the nighttime are very similar. This indicates that as long as the environment is favorable to the creation of convective cells (> 5dBZ), the life cycle of the cell intensity is not strongly affected by the diurnal cycle's change in the number of cells.

4.4.1 Signs of Internal Organization

Some investigation was done into the internal organization of the precipitation cells with regards to their direction of travel and the prevailing winds. The existence of cold pools in the marine stratocumulus environment was first analyzed with the VOCALS data set (Feingold et al. 2010, Terai and Wood 2013, Wilbanks 2013). An open question is; to what degree do marine stratocumulus cold pools initiate and organize drizzling cells? Potential evidence of strong cold pool organization at the scale of the precipitation core would be an asymmetric distribution of intensities inside the cell, with strong precipitation occurring near the leading edge and weaker near the trailing edge. In cells larger than 1 km², the 20% of the pixels farthest upstream were compared against the 20% of the pixels on the trailing edge.

For this purpose the upstream was considered to be towards the advection direction of the cells and downstream was away from the advection direction.

There appears to be no significant distinction between the forward and rearward portions of the cell. Figure 4.16 shows the frequency of forward minus rearward dBZ values as a function of track duration. Positive values indicate that the cell is more intense along the leading edge of the cell than it is along the trailing edge. Figure 4.16 shows a broad and nearly symmetric distribution of positive and negative values throughout the track duration. This indicates that while considerable asymmetries exist across the range of observed cells, the interaction between the mean flow and the cold pool does not appear to be a significant organizing factor to the internal structure of precipitation. This result may be a reflection of the relative small occurrence of strong cold pools in the vicinity of the ship during VOCALS (~70 cold pools identified by Wilbanks, 2013), rather than the absence of any possible effect.

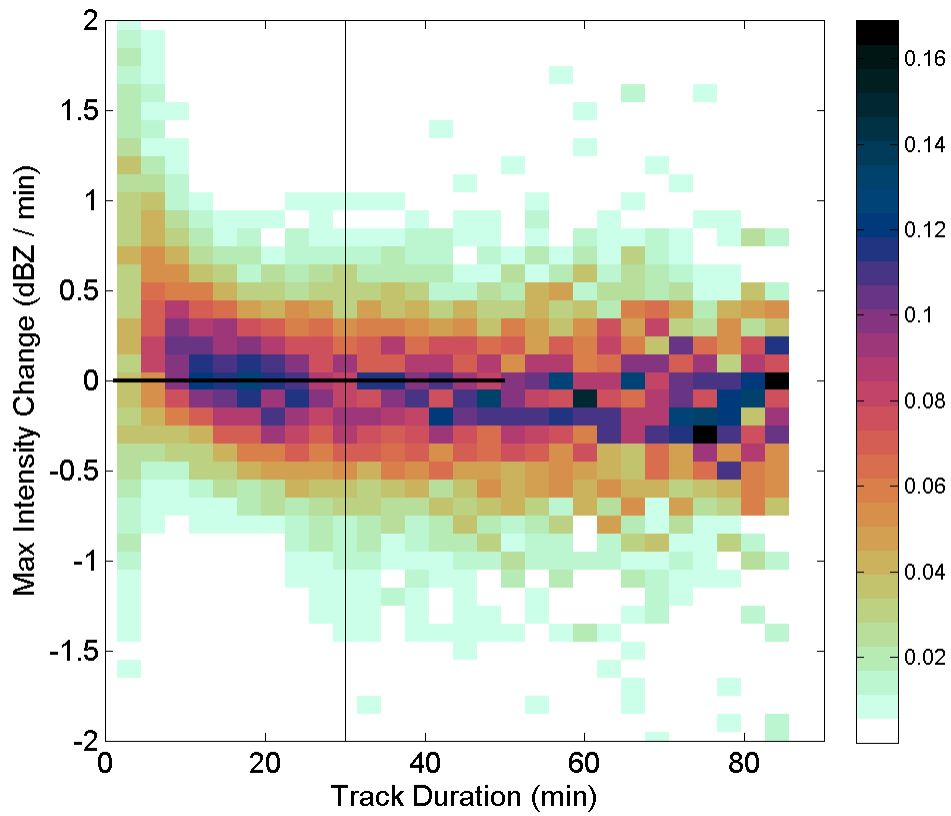


Figure 4.12: Frequency distribution of track intensity changes over observed lifetime for all tracks greater than 30 minutes. Max intensity change is filtered using a zero-phase, 9 minute moving average filter. Track duration is in minutes from the first observation of each cell. Frequencies have been normalized by the number of samples for each track duration column.

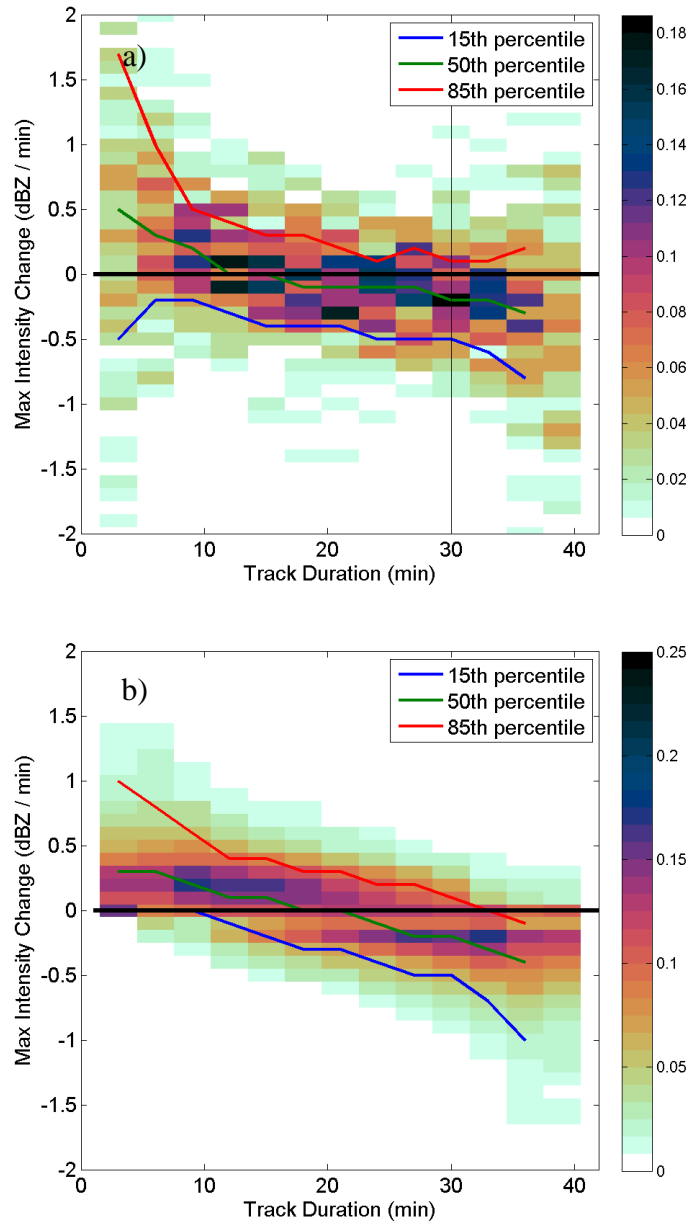


Figure 4.13: Frequency distribution of track intensity changes over time for real tracks (a) and simulated tracks (b) of length 42 minutes. Max intensity change is filtered using a zero-phase, 9 minute moving average filter. Track duration is in minutes from the first observation of each cell. Frequencies have been normalized by the number of samples for each track duration column.

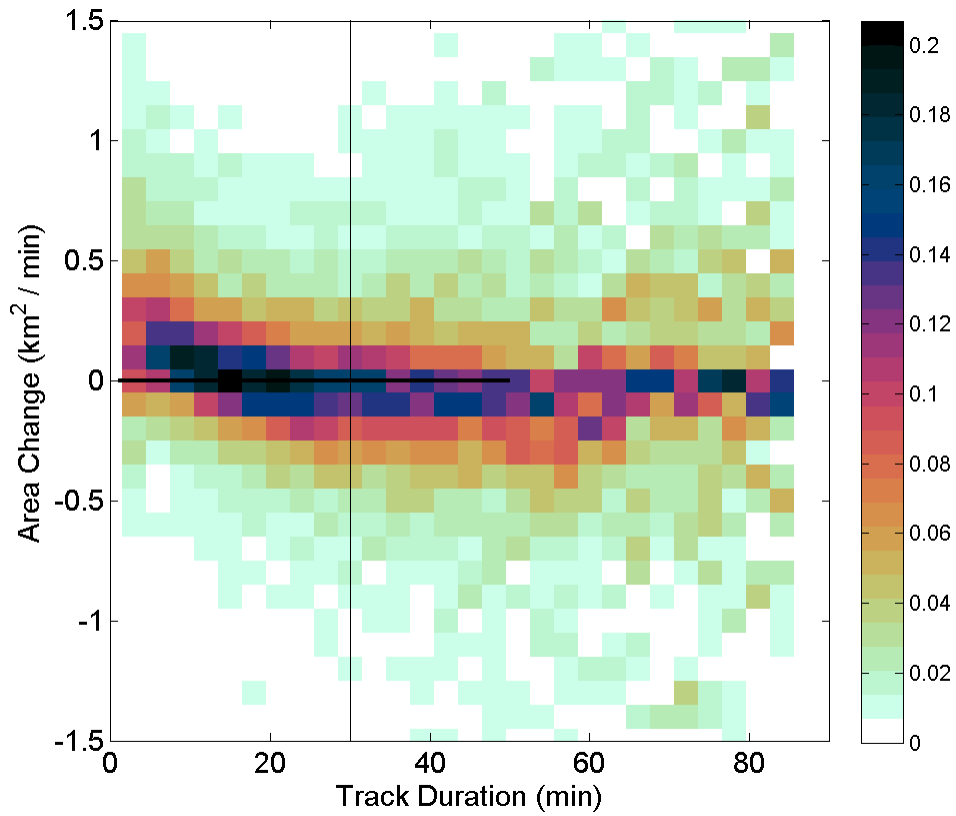


Figure 4.14: Frequency histogram of track area changes over observed lifetime for all tracks greater than 30 minutes. Max intensity change is filtered using a zero-phase, 9 minute moving average filter. Track duration is in minutes from the first observation of each cell. Frequencies have been normalized by the number of samples for each track duration column.

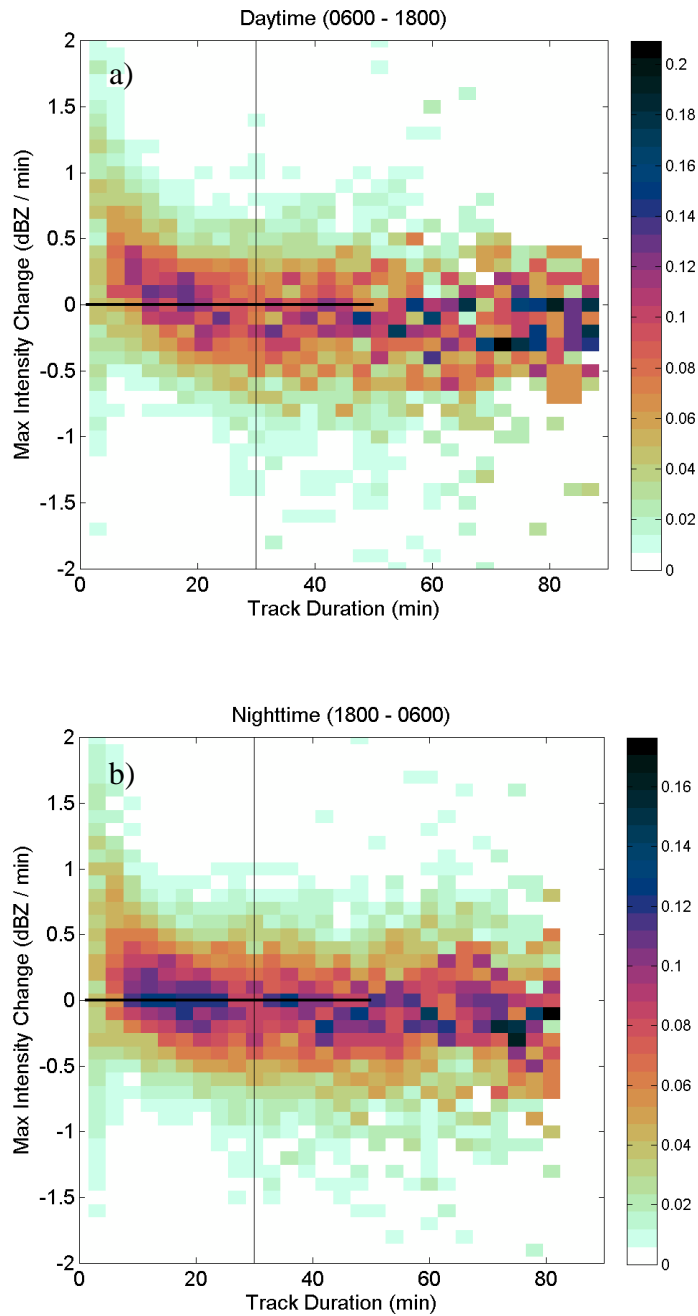


Figure 4.15: Frequency histograms of track intensity changes over observed lifetime for all tracks greater than 30 minutes separated into day (a) and night (b). Frequencies have been normalized by the number of samples for each track duration column.

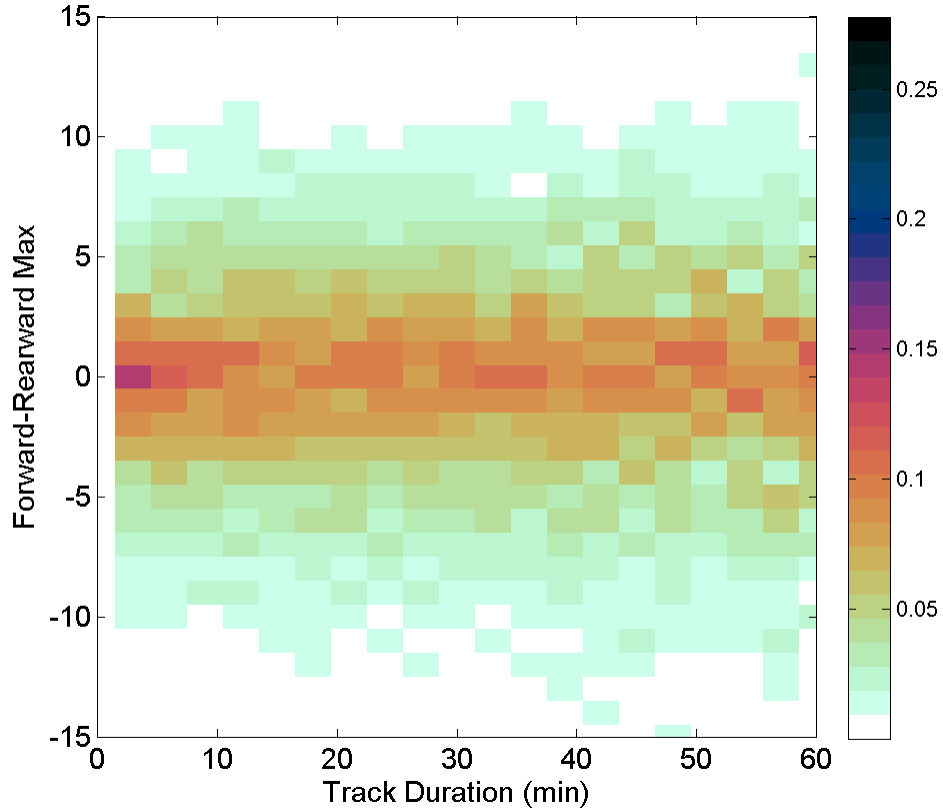


Figure 4.16: Frequency histogram of front-to-rear differential max intensity over observed lifetime for all tracks greater than 30 minutes. Forward and rearward are with respect to mean advection direction and comprise the 20 % of the pixels of the cell that are farthest forward or rearward. Frequencies have been normalized by the number of samples for each track duration column.

4.5 Mesoscale Structure and Cell Proximity

Examination of ship radar data over time shows that the cells often move together in the mean flow and appear to have some common, mesoscale organizing factors. In order to objectively determine the degree of mesoscale organization, the radar data were examined against a randomly generated field of cells. For each cell present in the domain the distance between all other cells was calculated, then minimum, unique value was recorded. A set of randomly generated points was created by sampling from a uniform distribution of points within a 120 km radius circle. Three random fields were created low spatial density (~6 cores in the domain), high spatial density (~50 cores in the domain) and an extremely high spatial density (~220 cores in the domain). The low and high densities represent “reasonable” cell densities similar to those observed while the “extreme” density provides a sort of upper bound to the analysis. To provide an analog to the radar data, the same geographic filters were applied to the randomly generated data including removing points within 8 km of the center or outside of 55 km from the center (see section 3.2). Figure 4.17 shows example distributions for each of the three random fields and a pair of observed cell locations. Notice that the observed cells are visually more clumped than the random low and high density fields. Figure 4.18 shows the distribution of the number of cells observed per frame across the data set. The low and high spatial densities represent values observed, while the extremely high case is used to come close to the observed cell proximities. For

each of the random densities 15000 instances were simulated and tested in order to get a robust set of values.

Figure 4.19 shows that the observed cells are much more likely to be closer together than the points from the two “reasonable” random fields, especially for proximities less than 8 km. The median proximity of observed cells in the VOCALS data is 5.5 km. This is significantly smaller than the median of proximities of the simulated high density field (9.5 km) and the simulated low density field (30 km). The four most commonly observed separations were between 2.5 and 4 km and represent 29 percent of the observed proximities but only 11 percent in the high density random field. In order for a uniformly random set of points to have a similar distribution of proximities to that of the observational data, approximately 330 points in the 120 km diameter domain would be needed.

The observed proximity of cells does not appear to change significantly with diurnal cycle or cloud condition (Figure 4.20). The most common distances remain in the 2.5 km to 4 km range with slight variations likely associated with the varying number of cells present overnight and in overcast conditions compared to daytime or broken conditions.

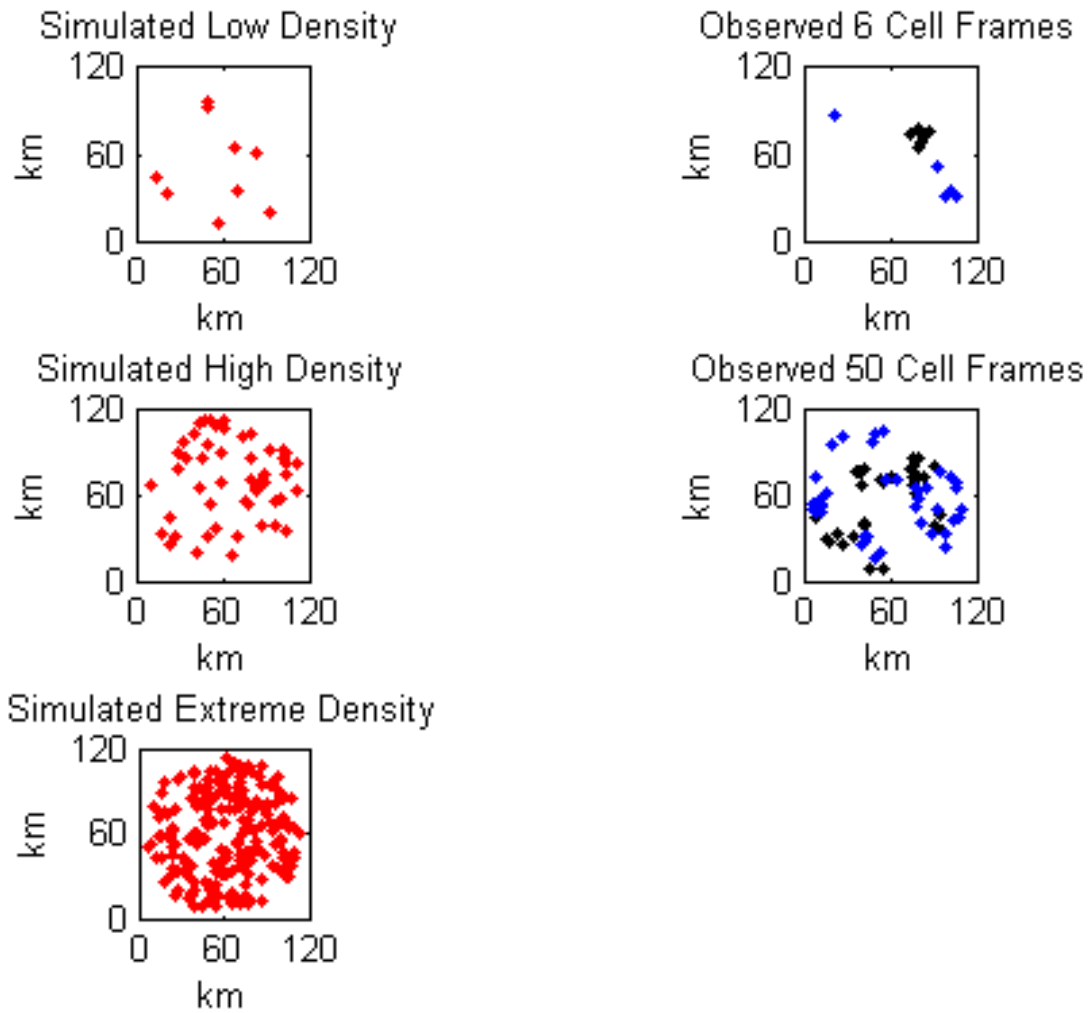


Figure 4.17: Cell location examples for the three random distributions (left column) and observed distributions (right column). For each of two cell densities (6 cells/frame and 50 cells/frame), two separate observed distributions are shown, each in a separate color (blue and black).

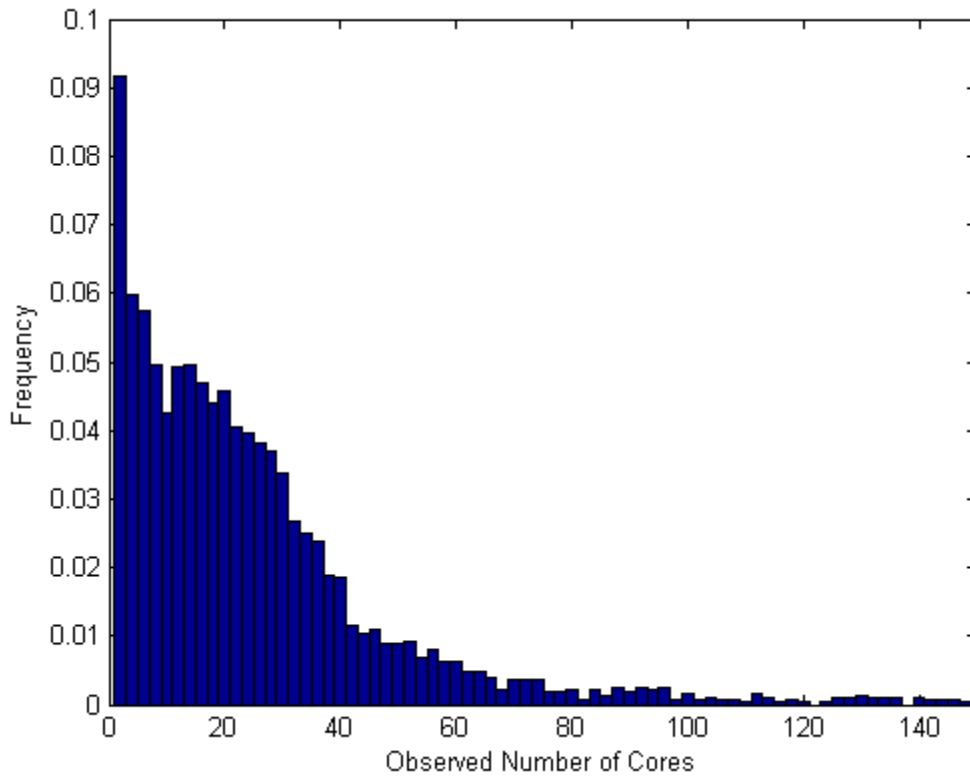


Figure 4.18: Histogram of number of precipitation cores per radar frame for frames with at least two cores present. Of the 10419 radar frames used in this analysis, 5699 (54%) frames had 2 or more precipitation cores.

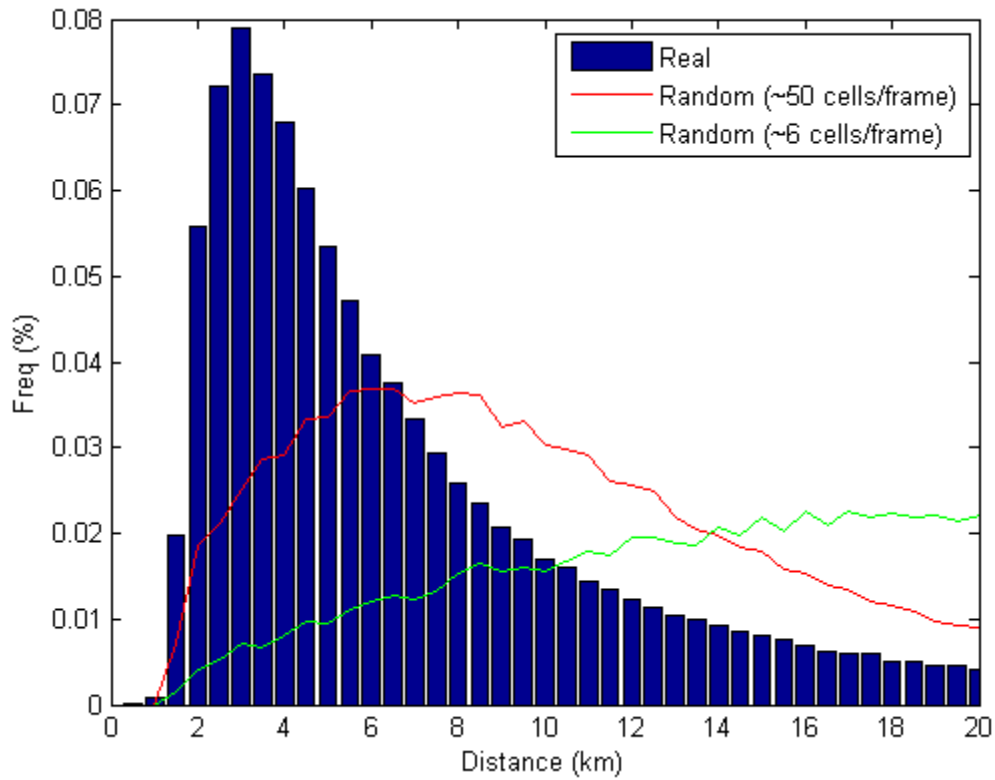


Figure 4.19: Distribution of unique minimum distances between observed cells (blue histogram) and two idealized uniform distributions of points (red and green lines). The distributions represent reasonable cell densities during high cell counts and low cell count times.

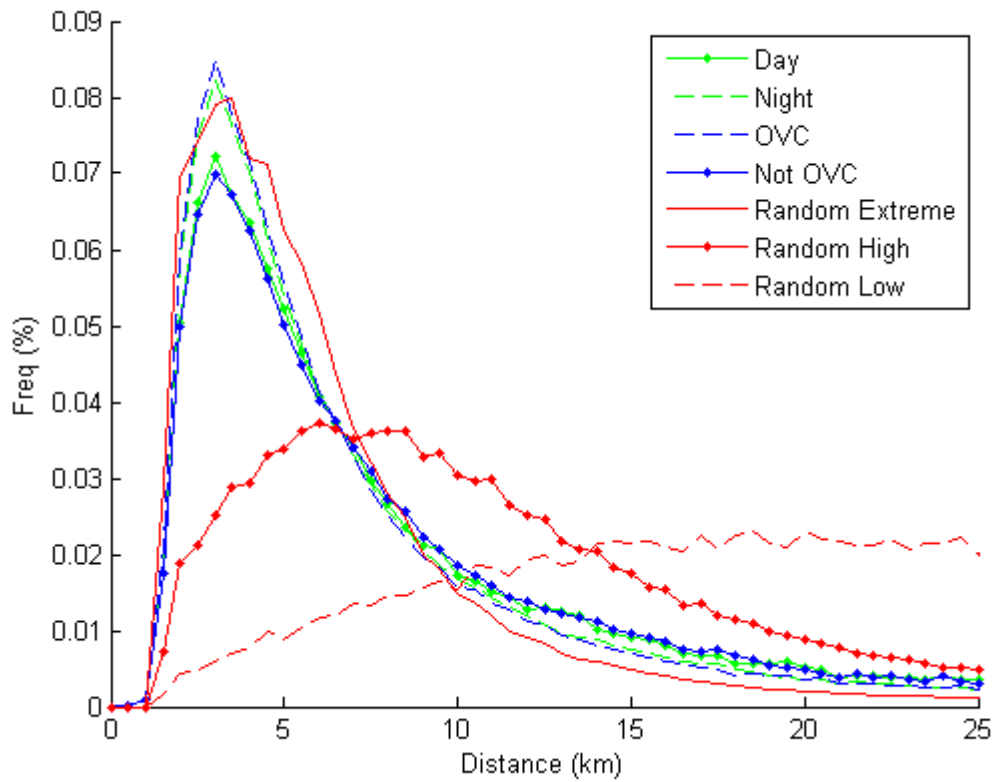


Figure 4.20: Probability density curves for unique minimum distances for different classifications; night versus day and overcast versus non-overcast. The proximities of cells appear similar across all four observed distributions. In red are three idealized cases of ~220, ~50, and ~6 cells per frame.

4.6 Comparisons to Other Types of Convection

The distributions of peak intensity, median area, and duration (figure above in stats section) all show log-normal distributions with varying amounts of positive skew. In the case of peak intensity and duration, the lower bound is an artifact of the minimum size and intensity criteria for cell identification, but the distribution is still apparent. The log-normal distributions of precipitating cell size and intensity have also been observed in convection in other regimes. The Rain in Cumulus over the Ocean field campaign (RICO) studied precipitation patterns in the North Atlantic trade wind region in the Caribbean (Raubert et al. 2007). Both the VOCALS and the RICO campaign took place in warm, moist environments with little to no large-scale, horizontal forcing. Both regions also have capping inversions that limit cloud growth to low altitudes.

For RICO's trade wind cumulus regime in the Caribbean, Trivej and Stevens (2010) found that both number and size distributions of precipitating cells were log-normal. The RICO and VOCALS results are compared in Figure 4.21 and 4.22. The important factor here is that the stratocumulus region exhibits a power-law like relationship for a broader range of cell sizes than the RICO environment, but with a similar overall relationship (Figure 4.21). Where RICO exhibited a fall-off in the relationship for cells larger than 10 km^2 , it appears that the VOCALS region has a strong power-law relationship until $\sim 100 \text{ km}^2$ areas are reached. A log-normal relationship between mean cell intensities compared to cell areas is

present also (Figure 4.22) however the relationship is significantly weaker for the VOCALS marine stratocumulus region compared to the trade cumulus observed in RICO. The increased instability and higher overall inversion level present in the trade cumulus environment compared to the marine stratocumulus environment (Mechem and Kogan 2003) is able to support greater cloud depths and stronger precipitation growth.

The log-normal distribution of the sizes of precipitation cores in the stratocumulus region also bears strong similarities to those found in weak tropical disturbances. Lopez (1975) performed tracking by hand, using photographs taken of an S-band airborne radar scope flying at cloud base through regions described as “cloud clusters” in the vicinity of Barbados. Lopez determined several cell characteristics (Lopez 1975, 1977) including the maximum area obtained by each precipitation region. Figure 4.21 shows fractional area contribution to the total precipitation area for a given maximum cell size. The fractional area contributions of cell sizes are quite similar between VOCALS and the Lopez study. Both have a strong log-normal contribution for cells between 30 and 200 km². The tapering off of smaller cells in the Lopez work is likely due to the relatively low spatial resolution of the radar equipment used in the era.

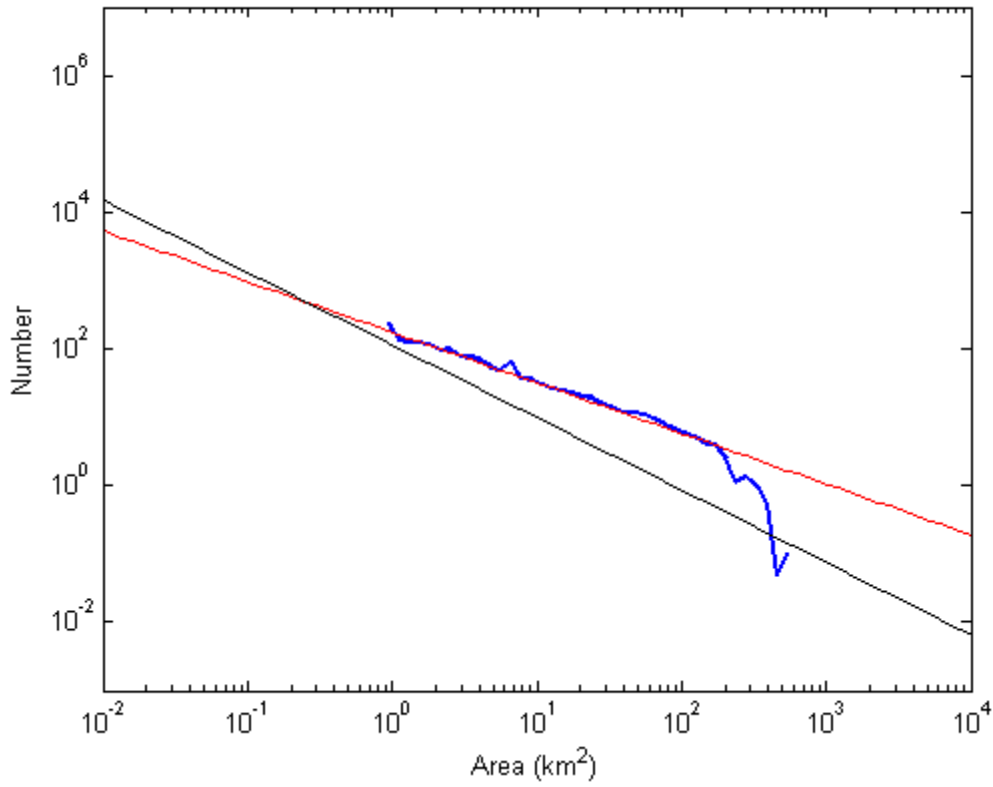


Figure 4.21: Log-log distributions of number of cells of a given area for VOCALS radar observations (blue) and the best fit lines for the 1 to 10 km² cells from RICO (Trivej and Stevens 2009) radar observations (black) and a similar best fit line for the VOCALS data (red).

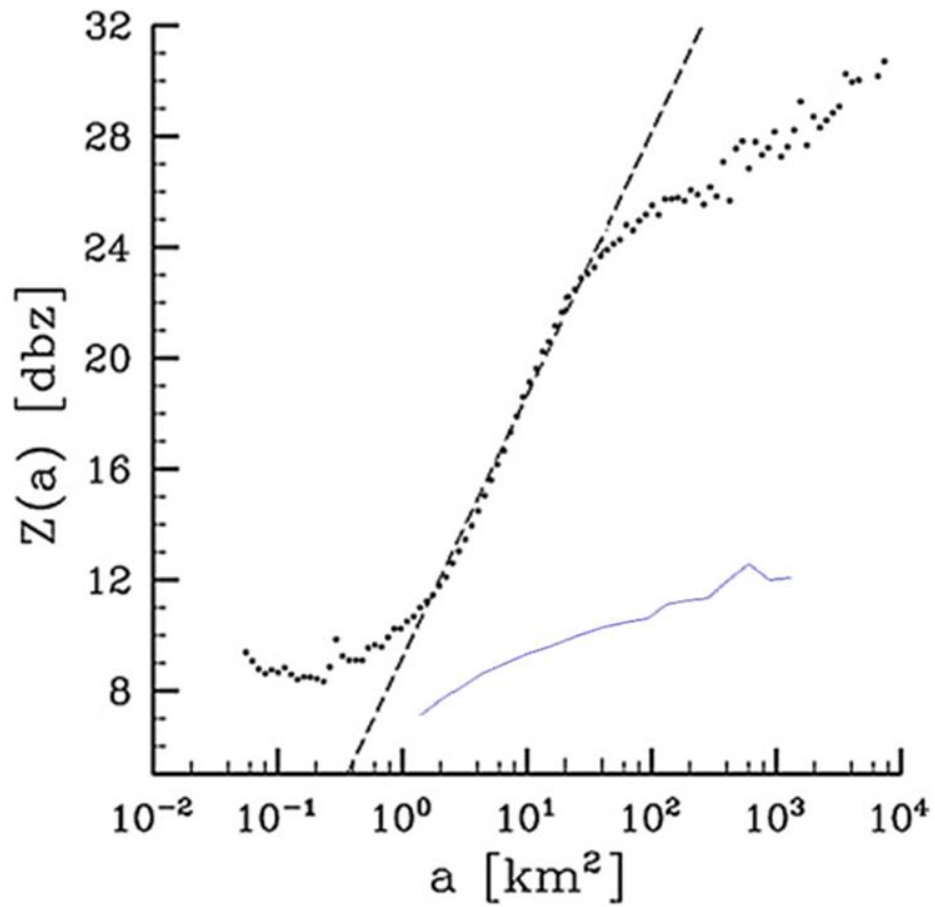


Figure 4.22: Distribution of mean cell intensity versus area on a log scale for VOCALS (blue) and RICO (black, reproduced from figure 8 from Trivej and Stevens 2010). Black dashed line is best fit from RICO for the 1 to 10 km^2 range.

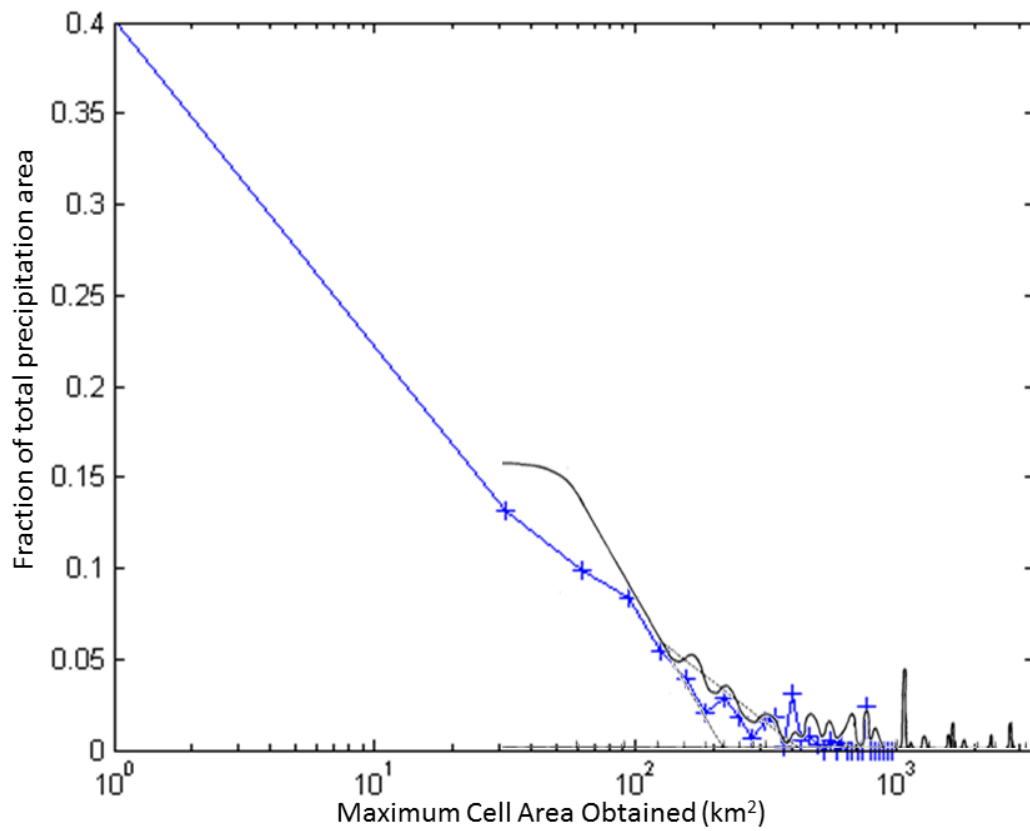


Figure 4.23: Histogram of the fractional contribution of total precipitation area for cells of a given area. Area bins used (blue crosses) are linearly spaced and identical to those used by Lopez (1975) with one additional bin existing below the minimum size threshold of that study. Lopez (1975) figure 3 is overlaid and to-scale.

4.7 Precipitation and Cloud Breakup

The relationship between precipitation and cloud breakup in stratocumulus environments is a current focus of research. Several studies (Stevens et al 2005, Wood et al 2011a) have observed regions of strong precipitation near regions of broken cloud, especially near the edges of POCs. Wood et al (2011a) uses an aircraft observed, cloud radar reflectivity data set to determine the relationship between cloud breakup and precipitation (Wood et al 2011a; their figure 5). The seven flight legs shown in Wood et al. (2011a) occurred between approximately 0320 and 0720 local solar time. The aircraft in the study repeatedly sampled the same “boundary cell” at the edge of a POC and five of the seven reference legs contain reflectivities of 21 dBZ or greater. With more than half of the cell observations containing 21 dBZ or greater intensities, the cell is at or above the 85th percentile for median cell intensities from the ship board, C-band observations. Berner et al. (2011) used a numerical simulation to recreate the observations shown in Wood et al (2011a). The simulation showed similarly intense (>20 dBZ) cells that matched those from the observations. In order to compare the observed (Wood et al. 2011a) and modeled (Berner et al. 2011) cell characteristics to the ship radar data set, the approximate size of the precipitation core was estimated by using the width of the sampled “boundary cell” as a rough diameter. Performing this calculation for the SC2 event in Wood et al (2011a) shows an approximate core diameter (region > 5 dBZ) of 8-10 km for an estimated area of 50 – 78 km². With

respect to the C-band observations 50 km^2 corresponds to the 98th – 99th % of the median area distribution and the 94th % of the maximum area attained distribution.

The cloud condition values used earlier were examined for how they changed overtime in relationship to both number of cells and total cell area. In order to reduce the number of possible transition types, the cloud condition was simplified to two values; either overcast or not overcast. All values originally observed as broken, scattered, or transition are considered broken (i.e. not overcast). Given two consecutive observations this reduces the possible outcomes to four events:

- 1) Start overcast, end overcast
- 2) Start overcast, end broken
- 3) Start broken, end overcast
- 4) Start broken, end broken

Events 1 and 4 represent no significant change to the cloud field in a 4 hour period. Event 2 represents a breakup of cloud and event 3 represents cloud increasing. These four types of cloudiness events are compared against 4-hr average precipitation area in Figure 4.24.

There are two distinct time scales involved in this analysis, that of the cloud state changing and that of the precipitation. The previous studies described above have made connections between precipitation cores with life times of 10's of minutes (30-90 minutes) having a significant effect on changing the cloud state over the course of several hours. The two primary pathways hypothesized for cloud breakup (aerosol depletion and/or sub-cloud

stabilization through evaporation) are both caused by significant amounts of liquid water precipitating out of the cloud layer. Sub-cloud evaporative cooling is strongest when precipitation is strongest (Burleyson et al 2013) while aerosol depletion requires large areas of precipitation in order to change the aerosol distribution of a cloud region. It is important to note that sub-cloud stabilization also occurs during the day independent of precipitation as a consequence of short-wave fluxes at cloud top offsetting long wave cooling (Bretherton 2010). Average precipitation area over each 4-hour period represents the liquid water flux on the timescales of the potential cloud breakup events. Other methods of precipitation volume estimation will be examined further in the paper being written with this work.

The first important detail is that regardless of cloud state transition no significant precipitation (> 5 dBZ) occurred 27% of the time. The occurrence of no significant precipitation was more common during periods of transitioning cloud condition (broken to overcast (36%), overcast to broken (29%)), and less common during steady state cloud conditions (remains overcast (19%), remains broken (23%)).

The cumulative frequency of the four types of events relative to precipitation area is shown in Figure 4.25. Cloud state transitioning from overcast to broken occurred 30% of the time with nearby significant precipitation in the area averaging greater than 63 km^2 . Contrasting this against when the cloud condition remained overcast, 47% of the time was the average precipitation area greater than 63 km^2 . This shows that if the cloud state is overcast now and we have a large area of precipitation in the vicinity, the cloud state is more likely to remain

overcast than become broken. If precipitation created cloud breakup than we would expect larger precipitation areas to be preferentially associated with cloud breakup instead of steady state cloudiness.

To further clarify the underlying forcing, the four event types were further separated into those occurring during the day and during the night (Figure 4.26). During overnight hours, the differences among the four different cloud condition transitions is minimal. Regardless of cloud transition event, about 50% of the time the average precipitation area was less than 15 km². During the daytime, the cloud states that were in transition showed cumulative distributions that are roughly the same slope (log-normal) but shifted up from the two unchanging cloudiness states, indicating that very little precipitation was observed in the vicinity of these cloud transitions. Less precipitation area during cloud transitions during the day is unlikely a function solely of less overall cloud area as the observations where the cloud cover started and remained broken show total precipitation areas similar to those periods that remain overcast. Strong precipitation in this region is also associated with thicker clouds and regions of lesser or no precipitation are associated with thinner clouds. This means that, in terms of cloud moisture, cloud breakup is likely easier in regions of no precipitation, while regions of strong precipitation have a larger amount of cloud water to remove.

Strong cells observed in prior work (Stevens et al 2005, Wood et al 2011a) and also seen in this data set, appear to occur infrequently overall and more frequently in broken cloud conditions. Additionally, while high intensity precipitation occurred most frequently

overnight in broken conditions, strong cells were observed throughout the data set in both day and night and in all cloud conditions (Figure 4.11). The hypothesis that precipitation is necessary but not sufficient to create cloud breakup, in marine stratocumulus (Wood 2011b, Mechoso 2013), is not supported by this data set. A significant portion (28%) of cloud breakup events occurred in the absence of any C-band radar observed precipitation cells and a majority (52%) of breakup events occurred with less than 10 km^2 of average precipitation area. Based on this analysis I would argue that a more realistic mantra for precipitation and cloud breakup would be “correlated but not required”.

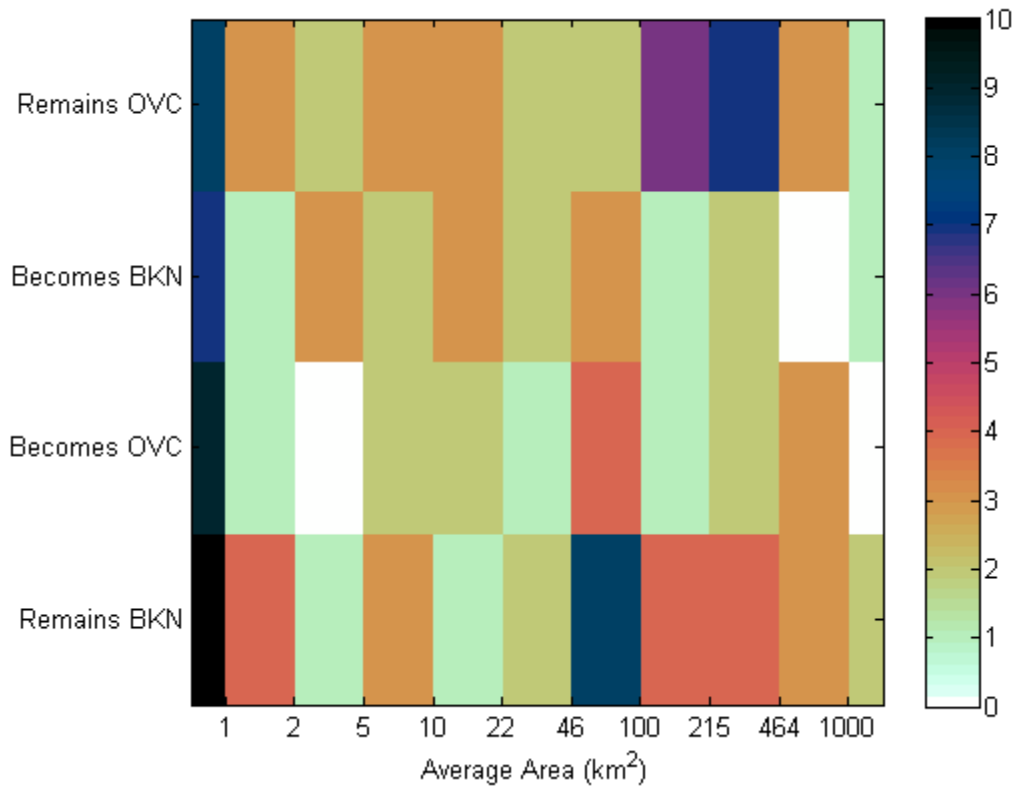


Figure 4.24: Observed number of each transition for each range of average areas shown. The left-most column represents average areas of less than 1 km² and periods with no precipitation observed. Based on total length of observation period, total number of 4 hour periods is 186.

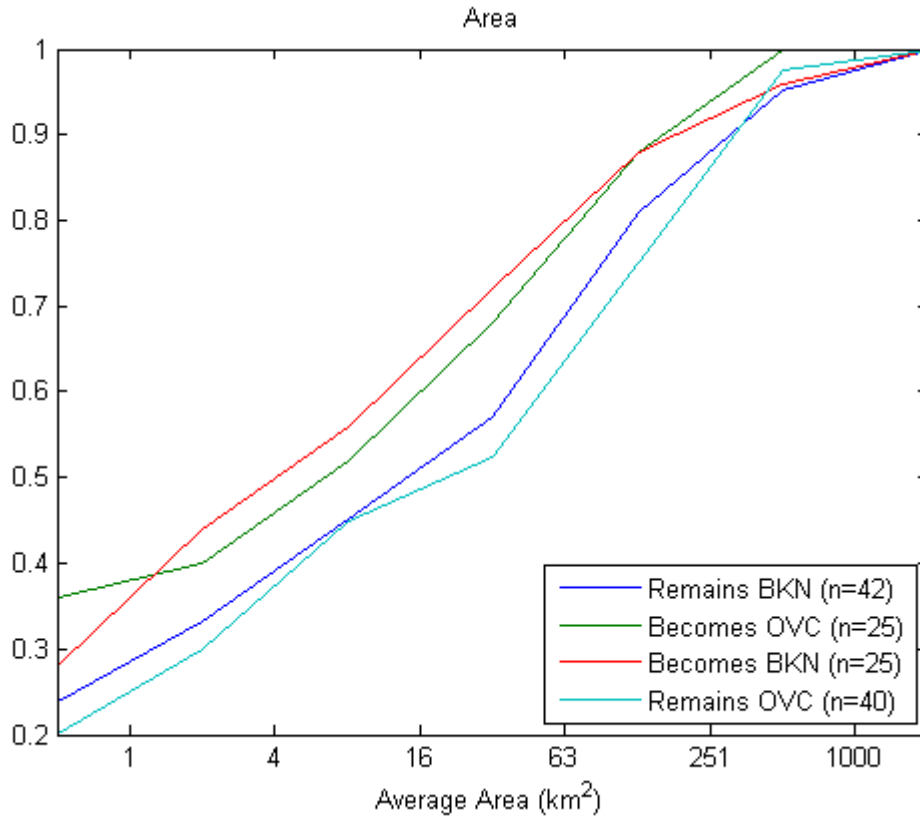


Figure 4.25: Cumulative probability that each transition occurred with average precipitation area less than or equal to the specified value. The location along the Y-intercept indicates the fraction of transitions that occurred with average precipitation area less than 1 km².

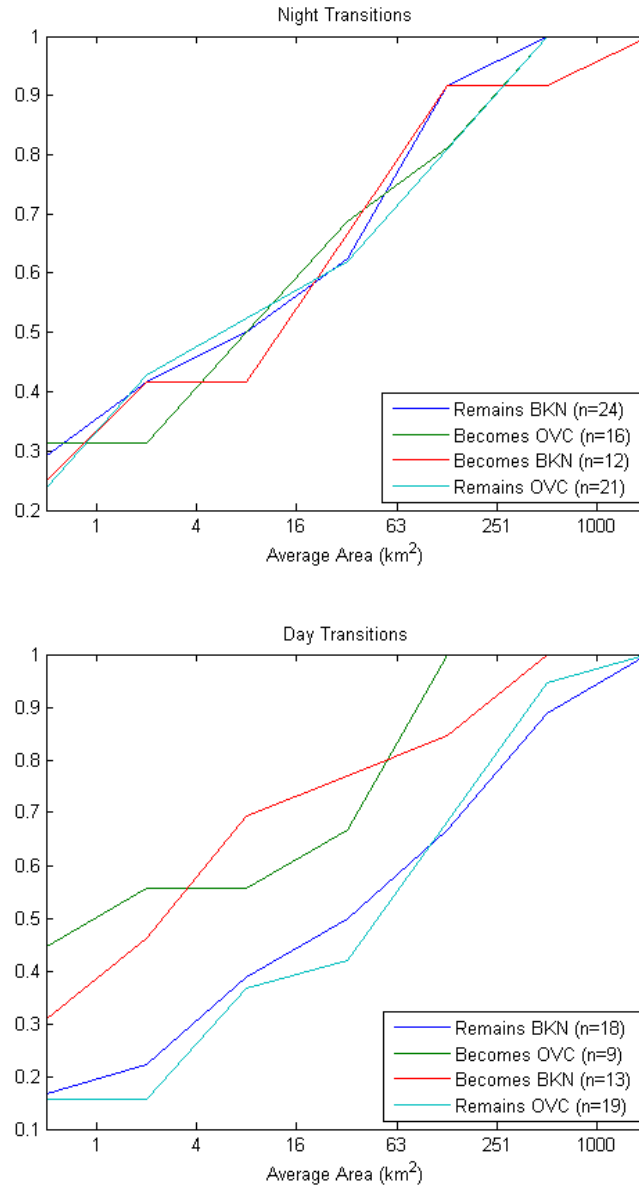


Figure 4.26: Cumulative probability for day (a) and night (b) that each transition occurred with average precipitation area less than or equal to the specified value. The location along the Y-intercept indicates the fraction of transitions that occurred with average precipitation area less than 1 km^2 .

Chapter 5

Conclusions

The centerpiece of this study is a high spatial and temporal resolution radar data set collected during the VOCALS-REX field campaign in the Southeast Pacific. Variability of drizzle cell characteristics and behavior over time are analyzed with respect to the diurnal cycle of cloudiness condition. The VOCALS ship-based data set used allows for a longer and more continuous observational period than previous studies (21 days compared to 6 days in EPIC, Comstock et al. 2007). Some aspects of drizzle cell life cycle are sensitive to time of day while others are not. Evidence for spatial organization was examined, with positive evidence found for mesoscale organization and no significant evidence found for strong, widespread cold pool forcing. Specific conclusions from this work are:

- 1) The onset of precipitation after sunset is delayed in regions of broken cloud conditions compared to overcast conditions. This fits with the conceptual model that the boundary layer is less coupled in regions of broken cloudiness versus overcast. Additionally, as the sun sets and the cloud layer recouples with the surface, some of the moisture being lifted from the near surface region would be used to grow the broken cloud horizontally, back towards an overcast state.
- 2) The three observed criteria of intensity, size, and duration are all positively correlated. As cells get more intense they tend to be larger and live longer. The

observed distributions should provide a bounding set to compare against modeled marine stratocumulus.

- 3) The median cell behavior is not strongly influenced by diurnal cycle or associated cloud condition. Cell count, a function of diurnal cycle, is the predominate influence on precipitation intensity and water flux.
- 4) The strongest cells were observed in broken cloud conditions overnight. The 85th % of peak intensities of the nocturnal, broken periods was substantially (8 dBZ) higher than the 85th% of peak intensities in nocturnal, overcast periods. This is confirmatory with previous studies (Stevens et al. 2005, Comstock et al 2007) that showed unusually strong precipitation in the vicinity of regions of broken clouds.
- 5) Cells tend to grow for a short period (~10-15 minutes) and then weaken over the remainder of their lives.
 - a. Cells that live longer than 30 minutes exhibit a similar early growth period, to shorter lived cells, with either slower decay periods or a pulsed life cycle after the initial growth.
 - b. Cell intensity life cycle does not change significantly with diurnal cycle or cloud condition.
- 6) Cells exhibit mesoscale organization and are not randomly distributed with respect to other cells. Cell proximities are significantly smaller than they would be if the field was random.
- 7) Marine stratocumulus precipitation cores have similar log normal distributions of intensity and area to other forms of convection. The areal contribution of

stratocumulus precipitation appears to follow a very similar pattern to that of both trade convection (RICO, Trivej and Stevens 2010) and weakly organized tropical convection (Lopez 1975). All types of convection are forced by buoyancy instabilities and not driven by synoptic or other strong horizontal gradients. All three types of subtropical convection have different inversion heights and strengths but otherwise similar distributions of moisture and temperature.

- 8) Precipitation area, and therefore total precipitation, is maximized during periods when the cloud condition remained steady state (either remained overcast or remained broken). During periods of cloud breakup strong cells were observed (conclusion 4), but the total water flux and total precipitation area were less overall than periods when the cloud state remained constant (either remaining overcast or remaining broken).

References

Albrecht BA. 1989. Aerosols, cloud microphysics, and fractional cloudiness. *Science* 245(4923):1227-30.

Allen G, Vaughan G, Toniazzo T, Coe H, Connolly P, Yuter SE, Burleyson CD, Minnis P, Ayers JK. 2013. Gravity-wave-induced perturbations in marine stratocumulus. *Q J R Meteorol Soc* 139(670):32-45.

Berner AH, Bretherton CS, Wood R, Muhlbauer A. 2013. Marine boundary layer cloud regimes and POC formation in an LES coupled to a bulk aerosol scheme. *Atmos Chem Phys Discuss* 13(7):18143-203.

Bony S, Colman R, Kattsov VM, Allan RP, Bretherton CS, Dufresne J, Hall A, Hallegatte S, Holland MM, Ingram W, et al. 2006. How well do we understand and evaluate climate change feedback processes? *J Climate* 19(15):3445-82.

Bretherton CS, Wood R, George RC, Leon D, Allen G, Zheng X. 2010. Southeast pacific stratocumulus clouds, precipitation and boundary layer structure sampled along 20° S during VOCALS-REx. *Atmos Chem Phys* 10(21):10639-54.

Bretherton CS, Uttal T, Fairall CW, Yuter SE, Weller RA, Baumgardner D, Comstock K, Wood R, Raga GB. 2004. The epic 2001 stratocumulus study. *Bull Amer Meteor Soc* 85(7):967-77.

Burleyson CD. 2013. Environmental controls on stratocumulus cloud fraction. NC State University.

Burleyson CD, De Szoeki SP, Yuter SE, Wilbanks M, Brewer WA. 2013. Ship- Based Observations of the Diurnal Cycle of Southeast Pacific Marine Stratocumulus Clouds and Precipitation. *J Atmos Sci* 72: 3876

Caldwell PM, Zhang Y, Klein SA. 2013. CMIP3 subtropical stratocumulus cloud feedback interpreted through a mixed-layer model. *J Climate* 26(5):1607-25.

Comstock KK, Bretherton CS, Yuter SE. 2005. Mesoscale variability and drizzle in southeast pacific stratocumulus. *J Atmos Sci* 62(10):3792-807.

Comstock KK, Yuter SE, Wood R, Bretherton CS. 2007. The three-dimensional structure and kinematics of drizzling stratocumulus. *Mon Wea Rev* 135(11):3767-84.

Comstock KK, Wood R, Yuter SE, Bretherton CS. 2004. Reflectivity and rain rate in and below drizzling stratocumulus. *Q J R Meteorol Soc* 130(603):2891-918.

- de Szoeke SP, Yuter S, Mechem D, Fairall CW, Burleyson CD, Zuidema P. 2012. Observations of stratocumulus clouds and their effect on the eastern pacific surface heat budget along 20°S. *J Climate* 25(24):8542-67.
- Dixon M and Wiener G. 1993. TITAN: Thunderstorm identification, tracking, analysis, and Nowcasting A radar-based methodology. *J Atmos Oceanic Technol* 10(6):785-97.
- Emanuel KA, David Neelin J, Bretherton CS. 1994. On large-scale circulations in convecting atmospheres. *Q J R Meteorol Soc* 120(519):1111-43.
- Feingold G, Koren I, Wang H, Xue H, Brewer WA. 2010. Precipitation-generated oscillations in open cellular cloud fields. *Nature* 466(7308):849-52.
- Frey M. 2013. Regional and interannual comparisons of marine stratocumulus precipitation. NC State University.
- Garreaud R and Munoz R. 2004. The diurnal cycle in circulation and cloudiness over the subtropical southeast pacific: A modeling study. *J Climate* 17(8):1699-710.
- George RC and Wood R. 2010. Subseasonal variability of low cloud radiative properties over the southeast pacific ocean. *Atmos Chem Phys* 10(8):4047-63.

Haralick, Robert M., and Linda G. Shapiro, Computer and Robot Vision, Volume I, Addison-Wesley, 1992, pp. 28-48.

Holder CT, Yuter SE, Sobel AH, Aiyyer AR. 2008. The mesoscale characteristics of tropical oceanic precipitation during kelvin and mixed Rossby Gravity wave events. *Mon Wea Rev* 136(9):3446-64.

Houze RA and Cheng C. 1977. Radar characteristics of tropical convection observed during GATE: Mean properties and trends over the summer season. *Mon Wea Rev* 105(8):964-80.

Johnson JT, MacKeen PL, Witt A, Mitchell ED, Stumpf GJ, Eilts MD, Thomas KW. 1998. The storm cell identification and tracking algorithm: An enhanced WSR-88D algorithm. *Wea Forecasting* 13(2):263-76.

Klein SA and Hartmann DL. 1993. The seasonal cycle of low stratiform clouds. *J Climate* 6(8):1587-606.

Lakshmanan V and Smith T. 2010. An objective method of evaluating and devising storm-tracking algorithms. *Wea Forecasting* 25(2):701-9.

Lopez RE. 1977. The lognormal distribution and cumulus cloud populations. *Mon Wea Rev* 105(7):865-72.

Lopez RE. 1976. Radar characteristics of the cloud populations of tropical disturbances in the northwest atlantic. *Mon Wea Rev* 104(3):268-83.

Lovejoy S. 1982. Area-perimeter relation for rain and cloud areas. *Science* 216(4542):185-7.

Mechem DB and Kogan YL. 2003. Simulating the transition from drizzling marine stratocumulus to boundary layer cumulus with a mesoscale model. *Mon Wea Rev* 131(10):2342-60.

Mechoso CR, Wood R, Weller R, Bretherton CS, Clarke AD, Coe H, Fairall C, Farrar JT, Feingold G, Garreaud R, et al. 2013. Ocean-cloud-atmosphere-land interactions in the southeastern pacific: The VOCALS program. *Bull Amer Meteor Soc* .

Morel C and Senesi S. 2002. A climatology of mesoscale convective systems over europe using satellite infrared imagery. I: Methodology. *Q J R Meteorol Soc* 128(584):1953-71.

Pincus R and Baker MB. 1994. Effect of precipitation on the albedo susceptibility of clouds in the marine boundary layer. *Nature* 372(6503):250-2.

Rotunno R, Klemp JB, Weisman ML. 1988. A theory for strong, long-lived squall lines. *J Atmos Sci* 45(3):463-85.

Stephens GL and Greenwald TJ. 1991. The earth's radiation budget and its relation to atmospheric hydrology: 2. observations of cloud effects. *J Geophys Res* 96:15325-40.

Stevens B, Vali G, Comstock K, Wood R, Van Zanten MC, Austin PH, Bretherton CS, Lenschow DH. 2005. Pockets of open cells and drizzle in marine stratocumulus. *Bull Amer Meteor Soc* 86(1):51-7.

Stevens B, Moeng C, Ackerman AS, Bretherton CS, Chlond A, de Roode S, Edwards J, Golaz J, Jiang H, Khairoutdinov M, et al. 2005. Evaluation of large-eddy simulations via observations of nocturnal marine stratocumulus. *Mon Wea Rev* 133(6):1443-62.

Terai CR and Wood R. 2013. Aircraft observations of cold pools under marine stratocumulus. *Atmos Chem Phys* 13(19):9899-914.

Trivej P and Stevens B. 2010. The echo size distribution of precipitating shallow cumuli. *J Atmos Sci* 67(3):788-804.

Wang H, Feingold G, Wood R, Kazil J. 2010. Modelling microphysical and meteorological controls on precipitation and cloud cellular structures in southeast pacific stratocumulus. *Atmos Chem Phys* 10(13):6347-62.

Wang H and Feingold G. 2009. Modeling mesoscale cellular structures and drizzle in marine stratocumulus. part I: Impact of drizzle on the formation and evolution of open cells. *J Atmos Sci* 66(11):3237-56.

Wilbanks MC. 2013. Near surface density currents observed in the southeast pacific stratocumulus-topped marine boundary layer. NC State University.

Wood R. 2005. Drizzle in stratiform boundary layer clouds. part I: Vertical and horizontal structure. *J Atmos Sci* 62(9):3011-33.

Wood R, Bretherton CS, Leon D, Clarke AD, Zuidema P, Allen G, Coe H. 2011. An aircraft case study of the spatial transition from closed to open mesoscale cellular convection over the southeast pacific. *Atmos Chem Phys* 11(5):2341-70.

Wood R, Mechoso CR, Bretherton CS, Weller RA, Huebert B, Straneo F, Albrecht BA, Coe H, Allen G, Vaughan G, et al. 2011. The VAMOS ocean-cloud-atmosphere-land study regional experiment (VOCALS-REx): Goals, platforms, and field operations. *Atmos Chem Phys* 11(2):627-54.